

1 **Including high frequency variability in coastal ocean acidification projections**

2

3 Yuichiro Takeshita*^{1,2}, Christina A. Frieder^{1,3}, Todd R. Martz¹, John R. Ballard¹, Richard A.
4 Feely⁴, Susan Kram¹, SungHyun Nam^{1,5}, Michael O. Navarro^{1,6}, Nichole N. Price^{1,7}, and Jennifer
5 E. Smith¹

6

7 1. Scripps Institution of Oceanography, University of California San Diego, La Jolla, CA 92093

8 2. now at: Carnegie Institution for Science, Stanford, CA 94305

9 3. now at: University of Southern California, Los Angeles, CA 90089

10 4. Pacific Marine Environmental Laboratory, NOAA, Seattle, WA 98115, USA

11 5. now at: Research Institution of Oceanography/School of Earth and Environmental Sciences,
12 Seoul National University, Seoul 151-742, Republic of Korea

13 6. now at: California State University Monterey Bay, Seaside, CA 93955, USA

14 7. now at: Bigelow Laboratory for Ocean Sciences, East Boothbay, ME 04544

15

16 * Corresponding Author: Carnegie Institution for Science, Department of Global Ecology,
17 Stanford, CA 94305 (ytakeshita@carnegiescience.edu)

18

19 Keywords: ocean acidification, acidification projection, pCO₂, upwelling margins, near-shore
20 habitats, calcium carbonate saturation state

21 Running Head: Unique Habitat Acidification Projections

22

23

24 **Abstract**

25 Assessing the impacts of anthropogenic ocean acidification requires knowledge of
26 present-day and future environmental conditions. Here, we present a simple model for upwelling
27 margins that projects anthropogenic acidification trajectories by combining high-temporal
28 resolution sensor data, hydrographic surveys for source water characterization, empirical
29 relationships of the CO₂ system, and the atmospheric CO₂ record. This model characterizes CO₂
30 variability on timescales ranging from hours (e.g. tidal) to months (e.g. seasonal), bridging a
31 critical knowledge gap in ocean acidification research. The amount of anthropogenic carbon in a
32 given water mass is dependent on the age, therefore a density-age relationship was derived for
33 the study region, and was combined with the 2013 Intergovernmental Panel on Climate Change
34 CO₂ emission scenarios to add density-dependent anthropogenic carbon to the sensor time series.
35 The model was applied to time series from four autonomous pH sensors, each deployed in the
36 surf zone, kelp forest, submarine canyon edge, and shelf break in the upper 100 m of the
37 Southern California Bight. All habitats were within 5 km of one another, and exhibited unique,
38 habitat-specific CO₂ variability signatures and acidification trajectories, *demonstrating the*
39 *importance of making projections in the context of habitat-specific CO₂ signatures.* In general,
40 both the mean and range of pCO₂ increase in the future, with the greatest increases in both
41 magnitude and range occurring in the deeper habitats due to reduced buffering capacity. On the
42 other hand, the saturation state of aragonite (Ω_{Ar}) decreased in both magnitude and range. This
43 approach can be applied to the entire California Current System, and upwelling margins in
44 general, where sensor and complementary hydrographic data are available.

45

46 **1 Introduction**

47 It has become increasingly apparent that upwelling systems, including the California
48 Current System (CCS), are particularly vulnerable to anthropogenic ocean acidification due to
49 their unique physical and chemical traits (Feely et al., 2008, 2010; Gruber et al., 2012; Hauri et
50 al., 2013a, 2013b). Upwelled waters have been isolated from the atmosphere and are naturally
51 elevated in CO₂ from remineralization of organic matter; depending on the age of the upwelled
52 water mass it may also contain anthropogenic carbon (Harris et al., 2013; Sabine et al., 2002).
53 Recent observations estimate the saturation horizon with respect to aragonite (depth at which Ω_{Ar}
54 = 1) along the CCS has shoaled by approximately 50 m since preindustrial times, and
55 undersaturated waters ($\Omega_{Ar} < 1$) have been observed at the surface near the California-Oregon
56 border during a strong upwelling event (Alin et al., 2012; Feely et al., 2008; Harris et al., 2013).
57 Furthermore, the rate of acidification (i.e. $\Delta\text{pH yr}^{-1}$) is expected to be significantly higher along
58 upwelling margins than observed in the surface open ocean (Bates et al., 2014; Gruber et al.,
59 2012; Hauri et al., 2013b; Leinweber and Gruber, 2013; Rykaczewski and Dunne, 2010) due to
60 the reduced buffering capacity of seawater at higher levels of CO₂ (Frankignoulle, 1994). This
61 effect has caused parts of the CCS to venture beyond the envelope (defined as: mean \pm 1 s.d.)
62 from modeled preindustrial Ω_{Ar} conditions (Hauri et al., 2013b). This is a concern because
63 organisms may need to survive outside of the environmental conditions to which they are
64 acclimatized, and the evolutionary potential for key ecological species to adapt to such rapid and
65 unprecedented changes is poorly understood. For example, a significant decrease in calcareous
66 benthic organisms was observed along a natural pH gradient near a cold volcanic CO₂ vent
67 (Hall-Spencer et al., 2008; Kroeker et al., 2011). However, some calcareous organisms such as
68 limpets seemed to have adapted to higher CO₂ levels compared to corals and mussels in the same

69 system (Rodolfo-Metalpa et al., 2011). Furthermore for upwelling margins, CO₂ co-varies with
70 other environmental stressors such as temperature and O₂ (Reum et al., 2015), making
71 predictions more difficult due to potential non-linear synergistic effects (Frieder et al., 2014).

72 A critical component in making accurate impact assessments of ocean acidification is the
73 development of robust, ecosystem-specific projections of future CO₂ conditions (Andersson et al.,
74 2013; Cai et al., 2011; Feely et al., 2009, 2010; McNeil and Matear, 2008; Sunda and Cai, 2012).
75 Development of surface, open-ocean acidification projections has been relatively straightforward,
76 as they rely on well-defined chemical principles of CO₂ equilibrium at the air-sea interface
77 (Byrne et al., 2010; Lauvset and Gruber, 2014). Models become more complicated when
78 attempting to resolve biological and physical processes that contribute significantly to the natural
79 variability of the system. For example, biologically mediated “enhanced acidification” was
80 identified in the northern Gulf of Mexico, causing significantly faster rates of acidification than
81 the open ocean (Cai et al., 2011). On many tropical coral reefs, seasonal patterns in CO₂ are
82 minimal, whereas the dominant frequency of variability occurs on diel and tidal frequencies
83 (Hofmann et al., 2011). On upwelling margins, both biological and physical processes contribute
84 to the observed natural variability of carbonate conditions (Fassbender et al., 2011).

85 One approach to develop region-specific ocean acidification projections is to apply an
86 eddy-resolving regional ocean model system (ROMS) coupled with a biogeochemical
87 component, as has been developed for the CCS (Gruber et al., 2011, 2012; Hauri et al., 2013b).
88 Such models have highlighted the importance of capturing physical and biological processes in
89 highly dynamic upwelling systems. The model simulations show complex spatiotemporal
90 variability (Hauri et al., 2013b), and predict that the frequency of “corrosive” upwelling events
91 will intensify in both magnitude and duration by the year 2050 (Hauri et al., 2013a). However,

92 the eddy-resolving ROMS project pCO₂ and saturation state conditions on a 5-km grid, whereas
93 many marine animals experience the environment on the scale of centimeters to meters. In
94 addition, regional models can largely resolve event-scale (weeks) and seasonal features, but
95 cannot capture fluctuations on diel to tidal time scales, which can be the dominant frequency of
96 variability in many near-shore environments (Duarte et al., 2013; Frieder et al., 2012; Hofmann
97 et al., 2011). Due to this discrepancy in both space and time, numerical models tend to
98 underestimate or entirely miss the high-frequency variability that exists for the microclimate of
99 organisms.

100 To transition from region-specific to habitat-specific ocean acidification projections, high
101 temporal resolution data from autonomous chemical sensors deployed across many habitat types
102 can be used to directly quantify the full range of present-day carbonate conditions (Harris et al.,
103 2013; Hofmann et al., 2011, 2014; Martz et al., 2014; Sutton et al., 2014). The CCS supports
104 many ecosystems that are of great ecological and economic value. In particular, there is great
105 habitat and species diversity near-shore on the shelf, which includes a large number of
106 commercially important invertebrates and fishes. Habitats in the region include bays and
107 estuaries, rocky and sandy intertidal, eelgrass beds and kelp forests, sub-tidal reefs, canyons and
108 extensive sandy sea floor. There are many endangered and harvested benthic organisms that
109 inhabit only one or a subset of these habitats.

110 Sensor data provide key observations for the mechanistic understanding of the controls
111 on environmental conditions, and are particularly needed for coastal marine environments where
112 complex physical and biological processes influence the observed variability. For example,
113 sensor data from a near-shore kelp forest in the southern CCS revealed that local biological
114 feedbacks and episodic upwelling events were the dominant drivers of CO₂ variability, with

115 pCO₂ fluctuating by 600 μatm at 17-m water depth (Frieder et al., 2012). This scale of variability
116 associated with near-shore environments is not captured by regional model simulations, but is
117 most relevant for organisms living inside the kelp forest.

118 Here, we present an anthropogenic ocean acidification model to project CO₂ chemistry
119 into the future by combining autonomous chemical sensor data, regional empirical relationships
120 for the CO₂ system (Alin et al., 2012), hydrographic data, and the atmospheric CO₂ record
121 (Keeling et al., 2005). This model was applied to four habitats ranging from the surface to 100-m
122 water depth and all within 5 km of each other in the Southern California Bight (SCB). Each site
123 showed distinct CO₂ variability signatures and acidification trajectories, highlighting the
124 importance of interpreting ocean acidification projections in the context of present and future
125 habitat-specific CO₂ signatures. Implications for future ocean acidification research are discussed.

126 **2 Methods**

127 *2.1 Study Sites*

128 Moored autonomous sensor packages SeapHOx or SeaFET (Bresnahan et al., 2014) were
129 deployed at four depths (4, 17, 30, and 88 m) within several distinct habitats on the San Diego
130 continental shelf for 1 year starting June 2012 (Figure 1). All sensors were deployed near the
131 seafloor; the three shallowest sensors were deployed within 3 m of the bottom, and the deepest
132 sensor was moored 12 m above the seafloor (Table 1).

133 A SeaFET was deployed at the Ellen Browning Scripps Pier 2 m above the benthos as a
134 part of the Scripps Ocean Acidification Real-time Monitoring Program. The sensor was located
135 approximately 400 m from the shore in the surf zone. Weekly discrete samples for total alkalinity
136 (TA) and dissolved inorganic carbon (DIC) were taken alongside the sensors for calibration and

137 quality control following standard protocols (Dickson et al., 2007). The sensor was serviced
138 every 1-2 months to remove biofouling organisms.

139 The La Jolla kelp forest is part of the South La Jolla State Marine Reserve and is
140 characterized by a dense population of *Macrocystis pyrifera*. The chemical variability in this
141 ecosystem is strongly influenced by regional physical processes (e.g., upwelling and
142 stratification) and local biological feedbacks (e.g., production and respiration). A SeapHOx was
143 deployed at 17 m in the southern portion of the kelp forest, 3 m above the bottom. The reader is
144 referred to *Frieder et al.*, 2012 for further details on site and deployment description.

145 The La Jolla canyon is a submarine canyon plunging from approximately 20 m to a depth
146 of 1000 m within several km from shore. A SeapHOx was deployed over a sandy bottom at the
147 southern canyon edge at 30 m depth within the Matlahuayl state marine reserve; the O₂ sensor
148 malfunctioned and thus is not included. The water in the La Jolla canyon is characterized by
149 higher salinity, and lower temperature, O₂, and pH (data not shown). Tidal energy in submarine
150 canyons is significantly amplified (Swart et al., 2011), bringing deep water from the canyon to
151 the canyon edge. Therefore, physical forcings are the dominant drivers for chemical variability at
152 this site (Navarro et al., 2013).

153 The Del Mar Buoy was first deployed in 2006 at 100 m off of Del Mar in northern San
154 Diego at the shelf break, and has provided continuous time series data (e.g. temperature, salinity,
155 oxygen, and current) at discrete depths (Frieder et al., 2012; Send and Nam, 2012). A SeaFET
156 sensor was deployed on the mooring at 88 m in 2011, and has provided a near-continuous time
157 series of pH since. Co-located sensors include temperature, salinity (SBE 37), and dissolved
158 oxygen (O₂; Aanderaa Optode). Water at this depth is isolated from the atmosphere and below
159 the euphotic zone, and thus influenced primarily by upwelling and tidal dynamics.

160 2.2 *Cruise data*

161 Hydrographic data were collected aboard R/V Melville during the student-led San Diego
162 Coastal Expedition cruises in June/July and December of 2012 (Figure 1). The SCB is
163 characterized by relatively weak (compared to the northern CCS), but nearly year-round
164 upwelling. However, there is a clear seasonal cycle based on climatological data, where
165 upwelling intensifies generally between April and August, with the maximum occurring in May
166 (Bograd et al., 2009). The cruises therefore corresponded with upwelling (June/July) and non-
167 upwelling (December) seasons. Water samples were collected at stations ranging from >100 km
168 from shore at 1200 m water depth, to within 5 km from shore at 30 m depth. Discrete samples
169 were analyzed for O₂, pH, and DIC; duplicate samples were collected during every cast.

170 Discrete samples for O₂ were collected and analyzed by titration using a custom-built
171 system (Martz et al., 2012). The titrant was standardized prior to and after each cruise using
172 KIO₃ standard solutions prepared in house (Fisher, lot 105595); no detectable drift was observed
173 for either cruise. Precision was $\pm 0.6 \mu\text{mol kg}^{-1}$ (duplicate n = 62, 1 s.d.), and the accuracy was
174 estimated to be $\pm 0.5\%$ because KIO₃ standards were not recrystallized (Emerson, 1999).

175 Samples for DIC and pH were collected in 150-ml or 250-ml Pyrex serum bottles (13-
176 mm neck) following standard procedures (Dickson et al., 2007). However, rather than leaving
177 headspace, the bottle was filled completely, and a gray butyl stopper was inserted to prevent gas
178 exchange and samples were analyzed within 4 hours of collection.

179 DIC samples were analyzed using custom-built system based on an infrared analyzer (LI-
180 COR 7000) similar to systems built by others (Friederich et al., 2002; O'Sullivan and Millero,
181 1998). The DIC measurements were calibrated using Certified Reference Materials provided by
182 the Dickson Lab at SIO, by applying a gain correction (slope) and assuming an offset of zero

183 (intercept). The reference materials were stored in CO₂ impermeable bags (3 L Scholle
184 DuraShield®), and were measured frequently throughout the cruise. The stability of the
185 reference material in the bag was verified by daily measurements of a new bottle; no drift was
186 observed. Precision and accuracy of the DIC measurements were $\pm 2.5 \mu\text{mol kg}^{-1}$ (duplicate n =
187 67, 1 s.d.).

188 Samples for pH were analyzed spectrophotometrically at 20 °C (Clayton and Byrne,
189 1993) using an automated system (Carter et al., 2013). The pH is reported on the total hydrogen
190 ion concentration scale. The indicator dye (m-cresol purple, ACROS Lot A0264321) was used as
191 received from the manufacturer without further purification. An offset was applied based on
192 measurements in certified Tris buffer provided by the Dickson Lab. The precision and accuracy
193 of the measurements were estimated to be ± 0.0015 (duplicate n = 86, 1 s.d.) and ± 0.02 (Liu et
194 al., 2011), respectively. TA and pCO₂ were calculated using CO2SYS (van Heuven et al., 2011)
195 using pH and DIC as inputs, and carbonic acid dissociation constants from *Mehrbach et al.*, 1973
196 refit by *Lueker et al.*, 2000.

197 2.3 *Sensor Data*

198 The SeapHOx and SeaFET sensor packages utilize a modified Honeywell Durafet III pH
199 combination electrode for high-frequency pH measurements (Martz et al., 2010). These sensor
200 packages have been successfully deployed in ecosystems worldwide (Frieder et al., 2012;
201 Hofmann et al., 2011; Kroeker et al., 2011; Martz et al., 2014; Price et al., 2012), and have been
202 shown to have excellent stability in seawater for months to years (Bresnahan et al., 2014). The
203 SeapHOx is an integrated sensor package that also consists of an Aanderaa 3835 oxygen optode,
204 and a Seabird SBE 37 Conductivity-Temperature sensor all plumbed into a pumped flow stream;

205 the SeaFET measures pH using a passively flushed cell. Sampling frequencies were 1 hr^{-1} or
206 greater at all depths.

207 All pH measurements were calibrated based on discrete TA and DIC samples taken
208 alongside the sensor, at minimum at the beginning and end of each sensor deployment ($n > 4$ for
209 every site), as recommended by the best practices (Bresnahan et al., 2014). The resolution of the
210 pH measurements is better than 0.0005 pH , stability is estimated to be better than 0.005 , and
211 accuracy is estimated to be ± 0.015 . Sensors were removed periodically for maintenance, but all
212 were deployed for > 50 days during both the upwelling and relaxation season.

213 At the surf zone (surface waters), a constant TA value of $2240 \mu\text{mol kg}^{-1}$ was assumed,
214 since discrete TA samples showed low variability (2240 ± 7 (1 s.d.) $\mu\text{mol kg}^{-1}$, $n = 57$). For the
215 three subsurface sensors, TA was estimated (TA^{est}) using a regional empirical relationship
216 developed for the CCS, with temperature and salinity as inputs (Alin et al., 2012); an offset of $+8$
217 $\mu\text{mol kg}^{-1}$ was applied to TA^{est} based on comparisons to discrete samples collected (root mean
218 squared error (RMSE) = $6 \mu\text{mol kg}^{-1}$, $n = 25$). This offset was a persistent feature over multiple
219 years (2010 – 2012), thus most likely reflecting a regional surface TA influence that is not
220 incorporated in the empirical relationship developed for the whole CCS. DIC, $p\text{CO}_2$, and Ω_{Ar}
221 were calculated using CO2SYS (van Heuven et al., 2011) using pH sensor data and TA^{est} as
222 inputs. Uncertainty for the calculated DIC, $p\text{CO}_2$, and Ω_{Ar} is pH-dependent, but on average is
223 estimated to be $\pm 13 \mu\text{mol kg}^{-1}$, $\pm 25 \mu\text{atm}$, and ± 0.04 , respectively. Daily range of sensor data
224 was calculated by first high-pass filtering the data with a 36 hour window, and then taking the
225 difference between the daily maximum and minimum. The mean daily range was then calculated
226 by averaging the resultant time series.

227 2.4 Modelling Future Carbonate Chemistry

228 2.4.1 Approach

229 The carbonate conditions were modeled by decreasing or increasing DIC while using TA
230 conditions from 2012. Modeled projections were made for preindustrial times and for year t ,
231 where t ranges between 2012 and 2100. The model presented here is based on the ΔC_t^* approach
232 (Gruber et al., 1996), but instead of using tracers to estimate the age of the water mass (e.g.
233 CFC's), we used the atmospheric CO₂ record as a quasi-age tracer. The age of the water mass
234 ranged between 0 and 50 years in this study region. Although this approach must be used with
235 caution, we demonstrate that our estimates are in good agreement with previously published
236 anthropogenic carbon inventory estimates using age tracer measurements in this region (Feely et
237 al., 2008; Sabine et al., 2002). In this model, it was assumed that ocean acidification is due to
238 anthropogenic CO₂ invasion through the air-sea interface alone. We also assumed that both the
239 path of a particular water mass between the subduction and upwelling site and the rate of
240 remineralization processes remain unchanged. Sensitivity to these assumptions is explored in the
241 Discussion.

242 The DIC of the modeled year t (DIC_t) is calculated by

$$DIC_t = DIC_{2012} + \Delta DIC_{anth} \quad (1)$$

243 where DIC_{2012} is the DIC observed in 2012, and ΔDIC_{anth} is the additional anthropogenic CO₂
244 that the water mass would have absorbed since 2012. Different formulations for ΔDIC_{anth} were
245 used for surface waters (i.e., above the seasonal mixed layer depth, defined here as $\sigma_\theta \leq 25.2$ kg
246 m⁻³) and subsurface waters ($\sigma_\theta > 25.2$ kg m⁻³), and are outlined below.

247 For surface waters, ΔDIC_{anth} was calculated as the difference in surface DIC between
248 year t and 2012. Surface DIC was calculated by assuming atmospheric equilibrium with TA =

249 2240 $\mu\text{mol kg}^{-1}$ (based on water samples from the Scripps pier) and using $\text{pCO}_{2,\text{atm}}$ projection
 250 under the 2013 IPCC RCP6.0 scenario (Hijioka et al., 2008). Although large deviations from
 251 equilibrium conditions are often observed in the coastal ocean due to upwelling and biological
 252 production (Hales et al., 2005), the mean pCO_2 calculated from sensor data at the surf zone was
 253 394 ± 43 (1 s.d.) μatm (Table 2), suggesting that the surface water at the study site was near
 254 atmospheric equilibrium.

255 For subsurface waters, $\Delta\text{DIC}_{\text{anth}}$ was quantified as the increase in DIC due to
 256 anthropogenic CO_2 when the water parcel was last in contact with the atmosphere. The mass
 257 balance of DIC for subsurface waters is:

$$\text{DIC} = \text{DIC}^\circ + \Delta\text{DIC}_{\text{bio}} \quad (2)$$

258 where DIC° is the preformed DIC, and $\Delta\text{DIC}_{\text{bio}}$ is the DIC added by remineralization processes
 259 in the ocean interior. DIC° can be expressed as the sum of DIC if it were in equilibrium with the
 260 atmosphere (DIC_{eq}) and the degree of air-sea disequilibrium due to slow gas exchange kinetics
 261 and biological processes ($\Delta\text{DIC}_{\text{diseq}}$):

$$\text{DIC}^\circ = \text{DIC}_{\text{eq}} + \Delta\text{DIC}_{\text{diseq}} \quad (3)$$

262 Since anthropogenic CO_2 only enters the ocean at the surface, the increase in DIC_{eq} represents
 263 the anthropogenic ocean acidification signal, $\Delta\text{DIC}_{\text{anth}}$, assuming $\Delta\text{DIC}_{\text{diseq}}$ is invariant with time.
 264 However, in order to use this approach, the age of the water parcel must first be quantified, as
 265 this determines the $\text{pCO}_{2,\text{atm}}$ with which it was last in contact.

266 The age of the water parcel was established by combining equations (2) and (3):

$$\text{DIC}_{\text{eq}}^{2012-\text{age}} = \text{DIC} - \Delta\text{DIC}_{\text{bio}} - \Delta\text{DIC}_{\text{diseq}} \quad (4)$$

267 where the superscript denotes the year at which the water parcel was last at the surface (i.e. equal
 268 to 2012 – age of the water mass). The age of the water mass was calculated by comparing the
 269 atmospheric CO₂ record to the pCO_{2,atm} that is necessary to generate $DIC_{eq}^{2012-age}$. ΔDIC_{diseq} was
 270 estimated from published values in the region (Section 2.4.3). Using this information, we
 271 calculated ΔDIC_{anth} by:

$$\Delta DIC_{anth} = DIC_{eq}^{t-age} - DIC_{eq}^{2012-age} \quad (5)$$

272 where the superscripts denote the year at which the water parcel was last at the surface, and age
 273 is the age of the water parcel. For example, if age = 30 yr and t = 2050, then CO₂ projections for
 274 the year 2020, would be used to calculate DIC_{eq}^{t-age} ; $DIC_{eq}^{2012-age}$ was calculated from equation
 275 (4). The ΔDIC_{anth} for subsurface waters was modeled for each projection year as a linear function
 276 of σ_θ , and the surface and subsurface ΔDIC_{anth} were connected assuming a two end member
 277 linear mixing between σ_θ 25.2 and 25.5 kg m⁻³ to prevent step changes (Figure 2).

278 2.4.2 Calculation of ΔDIC_{bio}

279 ΔDIC_{bio} was quantified following formulations in Sabine et al., 2002:

$$\Delta DIC_{bio} = r_{C:O}(AOU) - 0.5(TA_{obs} - TA^\circ + r_{N:O}(AOU)) \quad (6)$$

280 where $AOU = \text{Apparent Oxygen Utilization} = (O_{2,sat} - O_{2,obs})$, TA° is the preformed alkalinity,
 281 and the r 's are the elemental remineralization ratios (Anderson and Sarmiento, 1994). The
 282 oxygen saturation concentration ($O_{2,sat}$) was calculated using the equations in *Garcia and*
 283 *Gordon, 1992*, and TA° was estimated based on historical near-surface TA data in the Pacific
 284 (equation 3 in Sabine et al., 2002). Phosphate concentrations necessary to estimate TA° were not
 285 directly measured, but were estimated from a regional empirical relationship using historical data

286 (Supplementary Materials); the uncertainty in estimating phosphate using this approach
287 propagates to an error in TA° of $4 \mu\text{mol kg}^{-1}$.

288 2.4.3 *Estimation of $\Delta DIC_{\text{diseq}}$*

289 Making accurate estimates of $\Delta DIC_{\text{diseq}}$ is important because it is a source of large
290 uncertainty for anthropogenic carbon inventory calculations (Matsumoto and Gruber, 2005).
291 Traditionally, age of the water mass is quantified using tracers such as CFCs and then the
292 $\Delta DIC_{\text{diseq}}$ is subsequently calculated (Gruber et al., 1996; Sabine and Tanhua, 2010). However,
293 such tracer measurements were not made for this study. Alternatively, we estimated $\Delta DIC_{\text{diseq}}$
294 based on θ & S data to overcome this limitation (Sabine et al., 2002). The mean θ and S between
295 σ_θ of 25.5 and 26.5 kg m^{-3} were 10.0 $^\circ\text{C}$ and 33.9, respectively, resembling water type 1e in
296 Sabine et al. (2010) with a corresponding $\Delta DIC_{\text{diseq}} = -6.24 \mu\text{mol kg}^{-1}$, the value used in this
297 study.

298 2.4.4 *Calculation of the age of water parcel*

299 In order to estimate the age of the water mass, we use equation (4) to calculate
300 $DIC_{\text{eq}}^{2012-\text{age}}$, the DIC of the water parcel was in equilibrium with the atmosphere when it was
301 last at the surface (i.e. equal to 2012 – age of the water mass). Therefore the age of the water
302 mass can be calculated by comparing the atmospheric CO_2 record to the $p\text{CO}_{2,\text{atm}}$ that is
303 necessary to generate $DIC_{\text{eq}}^{2012-\text{age}}$. The latter was calculated from the fugacity of CO_2 of the
304 water mass when it was last in contact with the atmosphere at the time of subduction
305 ($f\text{CO}_{2,\text{eq}}^{2012-\text{age}}$), assuming 100% relative humidity, and barometric pressure of 1 atm [Dickson,
306 2007]. The year that the water parcel subducted was determined by matching the calculated
307 $\text{CO}_{2,\text{atm}}$ to the mean annual $\text{CO}_{2,\text{atm}}$ record (Keeling et al., 2005); the age is the difference

308 between 2012 and the calculated year (Figure 3). A relationship between σ_θ and the age was
 309 established by fitting a second order polynomial to the subsurface data ($n = 186$, $R^2 = 0.92$), and
 310 assuming the age of the surface water ($\sigma_\theta < 25.2$) is 0 (Figure 3). The non-zero age of the water
 311 that appears around $\sigma_\theta = 24.4 \text{ kg m}^{-3}$ corresponds to the shallow oxygen maximum layer that
 312 formed during the summer. However, since this density range is still shallower than the seasonal
 313 mixed layer, its age was considered to be 0. The age of the water ranged between 0 and 50 years
 314 between σ_θ of 25.2 and 26.5 kg m^{-3} .

315 2.4.5 Estimation of preindustrial DIC

316 In order to calculate the preindustrial DIC, equation (3) is written as:

$$DIC^\circ = DIC_{\text{eq}}^{\text{prein}} + DIC_{\text{anth}} + \Delta DIC_{\text{diseq}} \quad (7)$$

317 where DIC_{anth} represents the anthropogenic carbon present in the water parcel in 2012, and
 318 $DIC_{\text{eq}}^{\text{prein}}$ is the DIC of the water parcel if it were in equilibrium with $p\text{CO}_{2,\text{atm}} = 280 \text{ } \mu\text{atm}$.
 319 Combining equations (2) and (7) and rearranging gives

$$DIC_{\text{anth}} = DIC - \Delta DIC_{\text{bio}} - DIC_{\text{eq}}^{\text{prein}} + \Delta DIC_{\text{diseq}} \quad (8)$$

320 Calculated DIC_{anth} as a function of σ_θ is shown in Figure 4. Note that the values calculated
 321 here are in good agreement with published values using age tracers (Feely et al., 2008; Sabine et
 322 al., 2002) for higher σ_θ , but are significantly higher at lower densities. This is because the
 323 literature values were quantified using offshore subsurface waters, whereas our study region is
 324 near the coast along an upwelling margin, where subsurface waters are brought near the surface
 325 and are thus affected by surface processes. The agreement at higher density where surface
 326 influence is minimal demonstrates that the model presented here is capable of making accurate
 327 estimates of anthropogenic CO_2 . Furthermore, the comparison illustrates the importance of
 328 incorporating surface influence when making acidification projections in shallow, coastal

329 ecosystems. Preindustrial DIC (DIC_{prein}) was calculated by subtracting DIC_{anth} from DIC
330 observed in 2012. Preindustrial $p\text{CO}_2$, Ω_{Ar} , and pH were calculated using DIC_{prein} and TA
331 conditions from 2012.

332 **3 Results**

333 *3.1 Carbonate Chemistry Variability Observed in 2012*

334 The results are presented using pH, $p\text{CO}_2$, or Ω_{Ar} , since pH was directly measured, and
335 $p\text{CO}_2$ and Ω_{Ar} are commonly used as stress indicators for respiration (Brewer and Peltzer, 2009)
336 and calcification (Langdon et al., 2010), respectively. Across all four sites in 2012, $p\text{CO}_2$
337 increased with depth. In 2012, the mean $p\text{CO}_2$ in the surf zone was near atmospheric equilibrium
338 ($394 \mu\text{atm}$), while the mean $p\text{CO}_2$ at 88 m was $878 \mu\text{atm}$ (Table 2), and reached a maximum of
339 $1270 \mu\text{atm}$. The variability of $p\text{CO}_2$ also increased with depth (indicated by the s.d. of the time
340 series), which was only $43 \mu\text{atm}$ in the surf zone, but was $149 \mu\text{atm}$ at 88-m depth. The mean (\pm
341 1 s.d.) Ω_{Ar} decreased with depth; the mean Ω_{Ar} in the surf zone was 2.4 ± 0.25 , where it was 1.05
342 ± 0.18 at 88 m. Undersaturated conditions ($\Omega_{\text{Ar}} < 1$) were observed 48% of the time at 88 m in
343 2012, but were not observed at other sites. However, unlike $p\text{CO}_2$, the variability of Ω_{Ar} ,
344 indicated by the s.d., decreased with depth (0.25 at the surface to 0.18 at 88 m) (Table 2; see
345 Discussion). The mean pH decreased with depth; the mean pH in the surfzone was 8.05 , where it
346 was 7.73 at 88 m. The variability in pH increased with depth until 30 m, but decreased at 88 m
347 (Table 2).

348 Distinct, habitat-specific CO_2 signatures were observed at the four deployment sites
349 (Figure 5, Figure 6, and Figure 7). Here, we define habitat-specific CO_2 signatures as how CO_2
350 conditions varied in that habitat, regardless of biological or physical origin. In the surf zone, the
351 conditions were near atmospheric equilibrium, with intrusions of higher $p\text{CO}_2$ waters through

352 internal tidal bores, a common feature observed in shallow, upwelling environments (Booth et al.,
353 2012; Pineda, 1991); temperature and pH were correlated during these events (Supplementary
354 Figure S2). This leads to a high, mean daily range of CO₂ conditions (e.g. 96 μatm, 0.46, and
355 0.085 for pCO₂, Ω_{Ar}, and pH, respectively) (Table 3). However, the signature from the internal
356 bores usually only lasted several hours, and remained at near atmospheric equilibrium for the
357 large majority of the time. Higher occurrence of tidal bores were observed during the spring and
358 summer months relative to winter (Figure 5), consistent with previous observations (Pineda,
359 1991). The mean diel range of pCO₂ at the surf zone was significantly higher than measurements
360 made by a surface mooring located off shore in the SCB (Leinweber et al., 2009).

361 The mean (± s.d.) CO₂ conditions in the kelp forest and the canyon edge were similar,
362 and the s.d. for Ω_{Ar} and pH were the highest among the sites (Table 2). However, the timescales
363 of the variability were different, indicating that distinct processes control the CO₂ conditions in
364 these two habitats. For example, the mean daily range for all the variables was significantly
365 higher at the canyon edge compared to the kelp forest (Table 3). Submarine canyons are known
366 to amplify tidal energy (Navarro et al., 2013; Swart et al., 2011), and in fact, periodic variability
367 at the canyon edge occurred on semi-diurnal and diurnal cycles, indicative of tidal forcing.
368 Temperature and pH were correlated on these shorter timescales (Supplementary Figure 2),
369 further supporting the fact that the variability was dominantly driven by intrusion of cold, deep
370 waters from the canyon.

371 While tidal forcings and daily biological production are drivers for carbonate chemistry
372 in the La Jolla kelp forest, the largest variability occurred on event time scales (Frieder et al.,
373 2012); event time scales are defined as longer than a day, but shorter than several weeks. For
374 example, pH, pCO₂, and Ω_{Ar} regularly changed by up to 0.3, 250 μatm, and 1.3 on event time

375 scales, more than three times the mean daily range. Variability on event time scales is due to a
376 combination of changing water mass, stratification, and biological respiration (Frieder et al.,
377 2012). In addition, a clear seasonal pattern was observed at the canyon edge, where higher $p\text{CO}_2$
378 and lower pH and Ω_{Ar} were observed during the spring and summer months (upwelling season)
379 and lower $p\text{CO}_2$ and higher pH and Ω_{Ar} were observed during the fall and winter (relaxation
380 season). Due to incomplete data coverage, a seasonal trend at the kelp forest and pier sites could
381 not be discerned. The largest seasonal change among the four sites for Ω_{Ar} (~ 1) was observed at
382 the canyon edge; $p\text{CO}_2$ differed by roughly 200–300 μatm between the two seasons.

383 The shelf break experienced the highest mean CO_2 conditions, and the highest and lowest
384 s.d. for $p\text{CO}_2$ (149 μatm) and Ω_{Ar} (0.18), respectively (Table 2); the s.d. of pH (0.070) was lower
385 than the kelp forest (0.083) or the canyon edge (0.075). Variability on tidal, event, and seasonal
386 time scales were observed at this site (Figure 5, Figure 6, and Figure 7), as has been previously
387 reported for oxygen (Send and Nam, 2012). In general, upwelling on event time scales led to
388 greater changes in $p\text{CO}_2$ and pH than on tidal frequencies (Figure 5 and Figure 6). The largest
389 variability for all parameters occurred between the seasons, where a change in $p\text{CO}_2$, pH, and
390 Ω_{Ar} were approximately 350 μatm , 0.2, and 0.5, respectively. The close proximity of these four
391 sites demonstrates the wide variety of habitat-specific CO_2 signatures that exist over a small
392 spatial scale, especially in near shore environments.

393 3.2 Modeled Carbonate Chemistry

394 Each habitat showed distinct trends in both modeled mean and variability of $p\text{CO}_2$, pH,
395 and Ω_{Ar} owing to increased levels of anthropogenic DIC ($\Delta\text{DIC}_{\text{anth}}$) (Table 2). For example, the
396 mean $p\text{CO}_2$ at the surf zone (4 m), canyon edge (30 m), and shelf break (88 m) increased by 225,
397 435, and 738 μatm , respectively, from 2012 to 2100; this drastic difference in increased mean

398 pCO₂ is driven by different buffer factors due to depth differences among the sites. The increase
399 in variability (i.e. s.d.) was also larger at 88 m (97 μatm) compared to the surf zone (37 μatm),
400 although the largest increase occurred at the canyon edge at 30 m (126 μatm) (Table 2). Similar
401 trends were observed for mean pH, where the largest mean decrease in pH occurred at 88-m
402 water depth (0.26). However, the s.d. increased into the future for the three shallowest sites,
403 whereas the s.d. decreased at the shelf break (88 m). In contrast, the largest decrease in the mean
404 Ω_{Ar} occurred at the surface relative to the deeper sites, whereas the decrease in range was
405 equivalent across all depths.

406 The measured and modeled time series for pCO₂ and Ω_{Ar} at the shelf break for the year
407 2012 and 2100 are shown in Figure 8 and Figure 9. The variability of pCO₂ increases on both
408 seasonal and tidal time scales; the seasonal amplitude increases from approximately 350 to 650
409 μatm and the mean daily range increases from 110 to 325 μatm by 2100. This greater variability
410 is in addition to an increase in mean pCO₂ of > 700 μatm. On the other hand, the variability of
411 Ω_{Ar} on both seasonal and shorter time scales decreases. Furthermore, the shelf break is projected
412 to experience undersaturated waters over 90% of the time by 2060, compared to 48% in 2012.
413 Similar patterns were observed in the kelp forest as well, where both the mean conditions and
414 variability of pCO₂ increased, and Ω_{Ar} decreased (Figure 10). The largest variability at the kelp
415 forest occurred on timescales of days to weeks, and high frequency (< 1 day) variability was
416 significantly smaller than at the shelf break. Therefore benthic organisms at the kelp forest would
417 experience elevated CO₂ conditions for prolonged periods of time, with only intermittent
418 exposure to near-atmospheric conditions.

419 Preindustrial pCO₂ and Ω_{Ar} were compared to conditions observed in 2012 (Table 2). At
420 most sites, the observed pCO₂, pH, and Ω_{Ar} in 2012 were already outside of their preindustrial

421 variability envelopes (defined as mean \pm 1 s.d.), which is consistent with results from a previous
422 ROMS simulation in the CCS (Hauri et al., 2013b). These results suggest that all habitats studied
423 here have left, or are about to leave, the pCO₂, pH, and Ω_{Ar} conditions that were experienced
424 during preindustrial times. This is significant as organisms at these sites are now surviving in
425 conditions that are significantly different than the conditions under which their ancestors evolved.

426 The modeled habitat-specific pCO₂ and Ω_{Ar} conditions for preindustrial, 2012, 2060, and
427 2100 are shown in Figure 11. The histograms represent the full range of carbonate conditions at
428 each habitat that was captured by the sensors, which includes both the seasonal and high-
429 frequency variability. The shape of each distribution skews towards more “corrosive” conditions
430 at all sites as the model steps forward into the future. This translates to not only increases in
431 mean pCO₂, but also greater extremes and amount of time spent in extremes.

432 The projected pCO₂ and Ω_{Ar} envelopes (mean \pm s.d.) at each habitat throughout the
433 modeled period are shown in Figure 12. An increasing rate of change in pCO₂ (Δ pCO₂ yr⁻¹) is
434 observed, whereas Ω_{Ar} tends to decrease at a relatively constant rate. The rate of increase of
435 pCO₂ is higher than the projected atmospheric CO₂ increase at all subsurface sites. This indicates
436 that as ocean acidification progresses, the effects due to elevated pCO₂ are more likely to become
437 exacerbated with increasing depth. Mean Ω_{Ar} is projected to be < 1 at the shelf break by 2020,
438 and leave the 2012 variability envelope around 2070.

439 **4 Discussion**

440 *4.1 Changes in the Buffer Factors*

441 The general patterns of the acidification trajectories presented here can be explained by
442 changing buffer factors of seawater, as deeper sites are more strongly influenced by CO₂ rich
443 upwelled waters. The buffer factors Π_{pCO_2} , Π_{pH} , and Π_{CO_3} , are defined as

$$\Pi_{pCO_2} = \frac{\partial pCO_2}{\partial DIC}, \quad \Pi_{pH} = \frac{\partial pH}{\partial DIC}, \quad \Pi_{CO_3} = \frac{\partial CO_3^{2-}}{\partial DIC} \quad (9)$$

444 representing the change in each carbonate parameter with respect to a change in DIC
 445 (Frankignoulle, 1994). The effect of temperature on Π is small (< 10%) between 0-15 °C for the
 446 DIC and TA values observed here, thus subsequent values were calculated assuming a
 447 temperature of 10 °C, TA = 2240 $\mu\text{mol kg}^{-1}$, and salinity = 33.5 (Figure 13). The ability for
 448 seawater to buffer changes in pCO_2 diminishes under higher concentrations of DIC. For example,
 449 Π_{pCO_2} increases from 1.6 to 3.3 at the surface between 2012 and 2100 under the RCP6.0 scenario.
 450 However, since deeper waters are naturally elevated in DIC, this effect is more pronounced at the
 451 shelf break: Π_{pCO_2} increases from 6.2 to 12.3 during the same time interval. This explains why
 452 the surf zone had the lowest mean increase in pCO_2 (225 μatm) despite having the highest
 453 increase in DIC (82 $\mu\text{mol kg}^{-1}$) out of all of the sites. The shelf break on the other hand had the
 454 highest increase in pCO_2 (737 μatm) while having the smallest increase in mean DIC (77 μmol
 455 kg^{-1}) during the same time period. Furthermore, the increase in variability with depth can be
 456 explained as well, as the same biological and physical forcings on tidal to seasonal cycles cause a
 457 larger change in pCO_2 .

458 Changes in Π_{CO_3} can explain the patterns for Ω_{Ar} , since $[Ca^{2+}]$ and K_{SP} remain unchanged.
 459 Unlike Π_{pCO_2} , $|\Pi_{CO_3}|$ decreases at higher concentrations of DIC (Figure 13B); $|\Pi_{CO_3}|$ decreases
 460 from 0.62 to 0.57 at the surface, and 0.49 to 0.3 at 88 m between 2012 and 2100. This change in
 461 Π_{CO_3} explains both the decrease in rate and range of Ω_{Ar} as anthropogenic CO_2 continues to
 462 infiltrate the ocean.

463 The Π_{pH} follows a parabolic shape, where there is a maximum decrease in pH per DIC
 464 added (Figure 13C). In a pure carbonate solution, this maximum occurs when DIC = TA, but in

465 seawater it occurs at slightly lower DIC (Frankignoulle, 1994); this maxima occurs at DIC =
466 2225 $\mu\text{mol kg}^{-1}$ using the parameters listed above. Therefore we would expect to see a similar
467 trend for pH as pCO_2 , where greatest changes occur at depth relative to the surface as long as the
468 mean DIC is lower than this threshold. This condition is only met at the shelf break (88 m) near
469 the end of the century, thus as expected greater decrease in mean pH, and increase in variability
470 (i.e. s.d.) was observed with depth (Table 2). One exception was observed where the s.d.
471 decreased as ocean acidification progressed at the shelf break. This is because an increased
472 proportion of time is spent at greater DIC where Π_{pH} is past its maxima, leading to a smaller
473 variability in pH under the same changes in DIC. It is important to note that the buffer factor of
474 H^+ (Π_{H^+}) follows a similar pattern as pCO_2 , where it continues to increase as DIC increases
475 (Figure 13D). Therefore the rate of increase of $[\text{H}^+]$ will continue to increase as ocean
476 acidification progresses, thus biological responses to $[\text{H}^+]$ may become exacerbated in the future.

477 4.2 *Observed and Modeled Carbonate Chemistry Variability*

478 The carbonate conditions presented here are consistent with previous studies. For
479 example at the shelf break, Ω_{Ar} had a strong seasonal cycle, where undersaturated waters were
480 observed almost continuously throughout the upwelling season (Nam et al., 2015), and remained
481 supersaturated for the rest of the year. This is in good agreement with previous hydrographic
482 surveys in this region, where aragonite-undersaturated waters have been observed as shallow as
483 60 m during the beginning of the upwelling season (Feely et al., 2008), but were not observed in
484 the upper 100 m at the end of the upwelling season in this region (Bednaršek et al., 2014).
485 Furthermore, estimates based on empirical equations showed a similar seasonal pattern in Ω_{Ar} at
486 88 m, where undersaturated waters were observed every upwelling season (Alin et al., 2012).
487 However, undersaturated waters were not observed in the upper 30 m, unlike northern parts of

488 the CCS where undersaturated conditions are repeatedly observed at the surface during the
489 upwelling season (Bednaršek et al., 2014; Feely et al., 2008; Harris et al., 2013). Due to these
490 traits, the southern portion of the CCS is commonly considered less vulnerable to ocean
491 acidification compared to its northern counterpart. However, our results demonstrate that Ω_{Ar} as
492 low as 1.3 is routinely observed in the kelp forest (17 m), demonstrating the imminent threat of
493 anthropogenic ocean acidification to the southern CCS.

494 The subsurface habitats characterized in this study routinely experience Ω_{Ar} conditions
495 that have been shown to have non-lethal chronic effects on various bivalve larvae between Ω_{Ar} of
496 1.2 to 2.0 (Barton et al., 2012; Gaylord et al., 2011; Gazeau et al., 2011; Hettinger et al., 2012;
497 Waldbusser et al., 2015). However, the length of exposure to these unfavorable conditions varies
498 between habitats. For example, the organisms in the kelp forest would be exposed to low Ω_{Ar}
499 conditions for days to weeks, whereas large tidal variability at the canyon edge could result in
500 periodic exposure to low Ω_{Ar} conditions on the order of hours. Therefore the effects of low Ω_{Ar}
501 will largely depend on the reproductive timing and environmental variability that occurs on event
502 to seasonal time scales; the effects of exposure on various timescales are poorly understood.
503 Such events are expected to become more severe in the future (Hauri et al., 2013a), and thus
504 could lead to an increased rate of failed recruitment of bivalves and other keystone organisms
505 (Byrne et al., 2013).

506 It may be surprising that the mean diel range of pH was the smallest at the kelp forest
507 (Table 3), as one might expect a large diel cycle driven by photosynthesis and respiration in a
508 highly productive kelp forest. This is most likely because the sensor was deployed near the
509 benthos, below the most productive region of the forest. Frieder et al. 2012 observed
510 significantly larger diel pH variability closer to the surface (7 m depth) compared to near the

511 bottom (17 m depth; same as this study), demonstrating that the biologically driven diel cycle
512 diminishes with increasing depth within the canopy. Therefore it is important to keep in mind
513 that the results presented here are not reflecting kelp forest production dynamics, rather, reflect
514 conditions that are experienced by benthic dwelling organisms inside the kelp forest.

515 The trajectories are sensitive to the choice of the emission scenario (Figure 14). Trends
516 are similar at all depths, thus only the mean $p\text{CO}_2$ and Ω_{Ar} projections at the shelf break are
517 shown in Figure 14. The highest emission scenario (RCP8.5) diverges from the two intermediate
518 scenarios around 2030, while the lowest emission scenario (RCP2.6) diverges around 2050. The
519 two intermediate scenarios (RCP4.5 and RCP6.0) do not diverge significantly until 2070. The
520 delayed response to different atmospheric CO_2 trajectories occurs because upwelled waters have
521 spent several decades since they were last in contact with the atmosphere (Feely et al., 2008).
522 Therefore the anthropogenic ocean acidification trajectory for the Southern California Bight is
523 already determined for the next several decades, and any mitigation due to changing CO_2
524 emissions will be delayed.

525 The results presented here are site specific, and do not necessarily reflect conditions at all
526 kelp forests, canyon edges, and shelf breaks. However, if sensor pH data and corresponding
527 regional hydrographic surveys are available, then a $\Delta\text{DIC}_{\text{anth}-\sigma_\theta}$ relationship can be established
528 for that region and applied to the sensor data. For example, this approach can potentially
529 expanded to many regions for the CCS, using the North American Carbon Program West Coast
530 Cruise (Feely et al., 2008) and the $\Delta\text{DIC}_{\text{diseq}}$ for the Pacific Ocean (Sabine et al., 2002). If similar
531 data exist, then this approach can be expanded to other upwelling margins as well.

532 The Southern California Bight experiences a steady but weaker degree of upwelling
533 compared to the northern regions of the CCS, where upwelling events are more pronounced

534 (Bograd et al., 2009). These regions could experience more extreme conditions regularly, as well
535 as significantly higher variability of carbonate conditions (Harris et al., 2013). However, such
536 dynamics are poorly understood, and more high-frequency observations of carbonate parameters
537 along this system are needed. Source water properties must be characterized through
538 hydrographic surveys. Alternatively, for regions where such data for source waters are not
539 available, sensor data can be combined with either Global Circulation Model or ROMS outputs.
540 This approach will alleviate the cost associated with characterizing source waters, and to a large
541 degree will incorporate processes such as interannual variability, decadal changes in source
542 water properties, and reduced ventilation. It is critical that inorganic carbon sensors (e.g. pH or
543 pCO₂) are co-located with basic physical oceanographic measurements (e.g. T and S) to
544 determine source water properties especially for subsurface deployments.

545 4.3 Model Assessment

546 The sensitivity of the projected carbonate conditions to the assumptions made in the
547 model is explored here. For example, temperatures observed in 2012 were used to parameterize
548 the model. Sea surface temperature has increased over the past century due to climate change
549 (Smith et al., 2008), and is expected to continue. This will affect the CO₂ equilibrium
550 concentration (DIC_{eq}), but the effects are small and will reduce DIC_{eq} by only several $\mu\text{mol kg}^{-1}$.
551 Both pCO₂ and Ω_{Ar} are dependent on in situ temperature; the effects on Ω_{Ar} are negligible
552 ($\Delta\Omega/\Delta T < 0.01^\circ\text{C}^{-1}$), whereas $\Delta\text{pCO}_2/\Delta T$ increases at higher pCO₂ levels, and can be as large as
553 $60 \mu\text{atm } ^\circ\text{C}^{-1}$ at the end of the century, compared to $30 \mu\text{atm } ^\circ\text{C}^{-1}$ at present day at the shelf break.
554 These temperature dependencies will affect the mean conditions, but the magnitude of the
555 variability will be relatively unaffected. However, it should be noted that this simple error
556 analysis does not include any biological feedbacks that increased temperature or CO₂ may induce.

557 For example, phase shifts from kelp-dominated to algal turfs might be an outcome of sea surface
558 warming and acidification (Connell and Russell, 2010), with implications for habitat-scale
559 biogeochemical cycling. Likewise, higher temperatures may increase remineralization rates
560 along the path of the subducted water (Rivkin and Legendre, 2001), further enhancing
561 acidification.

562 TA conditions from 2012 were used to calculate $p\text{CO}_2$ and Ω_{Ar} for all years. Changes in
563 TA affect the buffer factors of seawater, thus, alterations in TA distribution will either speed up
564 or slow down the progression of ocean acidification. However, trends in TA along the CCS on
565 decadal time scales are unknown due to insufficient data. Reduced ventilation in high latitude
566 seas, altered precipitation patterns, and changes in surface calcification and water-column
567 dissolution rates would all lead to changes in upwelled TA conditions (Fassbender et al., 2011;
568 Lee et al., 2006). Quantifying these processes is difficult and out of the scope of this study.
569 Nevertheless, to demonstrate the magnitude of the uncertainty due to TA, $p\text{CO}_2$ was projected
570 for the year 2100 with a $+20 \mu\text{mol kg}^{-1}$ bias to TA. The effects were strongly dependent on
571 depth: mean $p\text{CO}_2$ was reduced by approximately 240, 130, and 70 μatm at 88 m, 30 m, and the
572 surface, respectively.

573 Finally, the model presented here projects future carbonate conditions by assuming the
574 dynamics that control the variability at each habitat (e.g. seasonal and episodic upwelling events,
575 internal waves and tides, and biological production and respiration) remain the same as 2012
576 conditions, and does not account for any variability that occurs on inter-annual to decadal
577 timescales. For example, changes in O_2 and pH on the continental shelf associated with
578 interannual climate events, such as El Niño, have been observed (Nam et al., 2011). However,
579 since 2012 did not correspond with a strong El Niño or La Niña phase, we believe that it was not

580 strongly biased by such events. Furthermore, recent evidence suggests that the proportion of
581 Pacific Equatorial Waters in the California Undercurrent has been increasing over the past
582 several decades, thus modifying the source water properties for upwelled waters onto the
583 continental shelf (Bograd et al., 2015). Since waters of equatorial origin observed between 100-
584 500 m are elevated in DIC and lower in O₂ (Bograd et al., 2015), it is expected that the Southern
585 California Bight will experience higher levels of acidification than predicted from this study if
586 this redistribution of water masses of equatorial origin continues. However, at this time, we lack
587 observations with sufficient longevity to predict how climate variability on interannual to
588 decadal time scales might modify the acidification trajectory over the course of the next century.
589 Sustained, high-frequency time series of inorganic carbon parameters are required to elucidate
590 such effects.

591 *4.4 Implications for Ocean Acidification Research*

592 In order to properly assess the impacts of anthropogenic ocean acidification through
593 laboratory manipulation experiments, the control and experimental conditions should accurately
594 reflect the study organism's present-day and future habitat conditions (McElhany and Busch,
595 2013; Reum et al., 2015). The most common control treatment used in ocean acidification
596 experiments for organisms found in the CCS was a pCO₂ value of ~400 μatm, reflecting
597 atmospheric conditions (compiled by Reum et al., 2015). However, our sensor data showed that
598 all subsurface habitats had significantly greater pCO₂ relative to the atmosphere (Table 2). For
599 example, the mean pCO₂ at the kelp forest is about 100 μatm greater than the atmosphere, and
600 routinely experiences conditions of more than 300 μatm above atmospheric. Therefore utilizing
601 atmospheric pCO₂ conditions for control treatments will necessarily underestimate the baseline
602 pCO₂ for organisms collected from subsurface habitats.

603 Recent studies that incorporate natural variability into ocean acidification experiments
604 observed modified responses relative to constant conditions (Dufault et al., 2012; Frieder et al.,
605 2014). However, the effect of natural variability on organismal response to ocean acidification,
606 especially through various life stages is still poorly understood. Our model results demonstrate
607 that variability trajectories are also habitat specific. For example, in the kelp forest, the
608 variability, approximated by the s.d., was 93 μatm in 2012, whereas this increased to 202 μatm
609 in 2100 (Table 2). Furthermore, despite having similar mean CO_2 conditions, the largest
610 variability was observed on event time scales in the kelp forest, whereas the dominant variability
611 occurred on tidal and seasonal cycles at the canyon edge. Therefore future ocean acidification
612 studies investigating the effect of natural variability should not only incorporate increasing
613 magnitude into their experimental design, but also consider variability patterns on appropriate
614 time scales.

615 Temperature and O_2 were tightly correlated with carbonate parameters across habitats
616 and various time scales (daily to seasonal) in this study (Figure 15); similar correlation has been
617 documented across the CCS in general (Reum et al., 2014, 2015). These parameters can
618 potentially act as additional stressors (Padilla-Gamiño et al., 2013) or stress reliefs (Gooding et
619 al., 2009) for ocean acidification. However, laboratory experiments incorporating the effects of
620 temperature (Gooding et al., 2009; Padilla-Gamiño et al., 2013) and O_2 (Frieder et al., 2014;
621 Navarro et al. *in prep*) have just started to be explored for the CCS, and no studies have been
622 conducted that incorporate all three variables in their experimental design. Future studies
623 investigating the synergistic effects of O_2 , temperature, and CO_2 should establish experimental
624 conditions based on environmental data (Figure 15). Although development of systems that can
625 manipulate individual parameters is challenging, important strides have been made to make such

626 experimental set ups accessible to the community (Bockmon et al., 2013). The development of
627 habitat-specific ocean acidification models provides a link between environment and laboratory
628 to facilitate interpretations of physiological responses to elevated CO₂ in the context of current
629 and future environmental conditions.

630 Discerning habitat-specific CO₂ signatures could lead to the discovery of local
631 populations that are more tolerant of future CO₂ conditions. For example, large high-frequency
632 variability of CO₂ could lead to a greater capacity for physiological and phenotypic plasticity, as
633 organisms are routinely exposed to a wide range of CO₂. The embryos of *Doryteuthis opalescens*,
634 an important fishery species in California, can tolerate low pH and O₂, perhaps due to the fact
635 that they routinely experience a wide range of pH and O₂ (Navarro, 2014). Furthermore, such
636 environmental conditions may be conducive for the existence of high CO₂ tolerant
637 subpopulations, allowing for adaptation to buffer some of the negative effects of ocean
638 acidification (Hofmann and Todgham, 2010). Alternatively, these populations could be living
639 near critical biological thresholds, as has been suggested for the thermal stress of some
640 organisms living in the intertidal (Somero, 2002). A massive failure in an oyster hatchery in
641 Oregon was linked to upwelling of high CO₂ waters during a critical life-stage of oyster larvae
642 (Barton et al., 2012), indicating the existence of CO₂ thresholds for some marine organisms
643 (Bednaršek et al., 2014). However, such thresholds may be dependent on species, life-stage,
644 and/or environmental history. As we begin to realize which populations of species and life stages
645 are living near acidification thresholds versus those that exhibit acidification tolerance,
646 implementation of habitat-specific acidification models can be used as a tool to aid protection,
647 management and remediation efforts of critical marine habitats now and in the future.

648 **5 Conclusions**

649 Here we have presented habitat-specific carbonate chemistry projections for four coastal
650 habitats along an upwelling margin. The projections were generated by combining high-
651 frequency sensor measurements, a regional empirical relationship for TA, hydrographic survey
652 data to quantify source-water properties of upwelled waters, and the atmospheric CO₂ record.
653 Even though the four habitats were within 5 km of one another, distinct habitat-specific
654 variability signatures and acidification trajectories were observed. These results reveal the
655 existence of highly variable CO₂ signatures within a small geographic area, and the potential for
656 discoveries of habitats that could act as refugia from ocean acidification. Changes in the buffer
657 factors largely explained the observed patterns; however, local biological feedbacks could also
658 produce a large acidification signal. In all habitats studied, carbonate conditions have left, or are
659 leaving preindustrial variability envelopes. Model projections suggest that anthropogenic ocean
660 acidification will continue to progress in the CCS and other upwelling margins over the next
661 several decades regardless of any changes in CO₂ emissions; any impacts from reduced
662 emissions will only be observed mid-century and beyond. This demonstrates the urgency of the
663 situation, and this delayed response must be taken into account when assessing the impacts of
664 ocean acidification and developing mitigation and monitoring strategies.

665 **6 Acknowledgements**

666 Hydrographic data and kelp forest time series data are available at BCO-DMO project
667 SeapHOx (<http://www.bco-dmo.org/project/2122>). Sensor time series data are available for the
668 Del Mar buoy at <http://mooring.ucsd.edu>, and upon request for the Scripps Pier
669 (smithj@ucsd.edu).

670 We would like to thank the University of California Ship Funds for providing ship time
671 for maintenance of the Del Mar Buoy and the San Diego Coastal Expedition cruises. We thank
672 Emily Kelly for DIC analysis at sea, and all of the ship crew and volunteers that aided in sample
673 collection. We would like to thank Emily Donham for providing discrete TA data from the kelp
674 forest. The Del Mar Buoy platform has been maintained by the Ocean Time-series Group
675 (<http://mooring.ucsd.edu>); we acknowledge their efforts to continuously collect and maintain the
676 time-series data. The canyon edge deployment was supported by the NOAA Grant
677 #NA10OAR4170060 and the California Sea Grant College Program Project #R/CC-04. The kelp
678 forest deployment was supported by NSF-OCE Award No. 0927445. We would also like to
679 thank the Ellen Browning Scripps Foundation, the Scripps Family Foundation, the Bohn and
680 Grand families, and the California State Water Board for financial support for the Scripps Ocean
681 Acidification Real-time Monitoring Program. S. Nam was partly supported by the Research
682 Resettlement Fund for the new faculty of Seoul National University and Korean Ministry of
683 Oceans and Fisheries through EAST-I program. Financial support for Richard A. Feely was
684 provided by the National Oceanic and Atmospheric Administration under the NOAA Ocean
685 Acidification Program and the Climate Observations Division of the NOAA Climate Program,
686 Contribution Number 4313 from the NOAA Pacific Marine Environmental Laboratory. The
687 statements, findings, conclusions and recommendations are those of the authors and do not
688 necessarily reflect the views of California Sea Grant, state agencies, NOAA, NSF or the U.S.
689 Department of Commerce.

690

691 **Literature Cited**

- 692 Alin, S. R., Feely, R. A., Dickson, A. G., Hernández-Ayón, J. M., Juranek, L. W., Ohman, M. D.
693 and Goericke, R.: Robust empirical relationships for estimating the carbonate system in the
694 southern California Current System and application to CalCOFI hydrographic cruise data (2005–
695 2011), *J. Geophys. Res.*, 117(C5), C05033, doi:10.1029/2011JC007511, 2012.
- 696 Anderson, L. A. and Sarmiento, J. L.: Redfield ratios of remineralization determined by nutrient
697 data analysis, *Global Biogeochem. Cycles*, 8(1), 65–80, 1994.
- 698 Andersson, A. J., Yeakel, K. L., Bates, N. R. and de Putron, S. J.: Partial offsets in ocean
699 acidification from changing coral reef biogeochemistry, *Nat. Clim. Chang.*, 3(11), 1–6,
700 doi:10.1038/nclimate2050, 2013.
- 701 Barton, A., Hales, B., Waldbusser, G. G., Langdon, C. and Feely, R. A.: The Pacific oyster,
702 *Crassostrea gigas*, shows negative correlation to naturally elevated carbon dioxide levels:
703 Implications for near-term ocean acidification effects, *Limnol. Oceanogr.*, 57(3), 698–710,
704 doi:10.4319/lo.2012.57.3.0698, 2012.
- 705 Bates, N. R., Astor, Y. M., Church, M. J., Currie, K., Dore, J. E., Gonzalez-Davila, M.,
706 Lorenzoni, L., Muller-Karger, F., Olafsson, J. and Santana-Casiano, J. M.: A time-series view of
707 changing surface ocean chemistry due to ocean uptake of anthropogenic CO₂ and ocean
708 acidification, *Oceanography*, 27(1), 126–141, 2014.
- 709 Bednaršek, N., Feely, R. A., Reum, J. C. P., Peterson, B., Menkel, J., Alin, S. R. and Hales, B.:
710 *Limacina helicina* shell dissolution as an indicator of declining habitat suitability owing to ocean
711 acidification in the California Current Ecosystem., *Proc. R. Soc. B Biol. Sci.*, 281(1785),
712 20140123, doi:10.1098/rspb.2014.0123, 2014.
- 713 Bockmon, E. E., Frieder, C. A., Navarro, M. O., White-Kershek, L. A. and Dickson, A. G.:
714 Technical note: controlled experimental aquarium system for multi-stressor investigation of
715 carbonate chemistry, oxygen saturation, and temperature, *Biogeosciences*, 10(9), 5967–5975,
716 doi:10.5194/bg-10-5967-2013, 2013.
- 717 Bograd, S. J., Buil, M. P., Lorenzo, E. Di, Castro, C. G., Schroeder, I. D., Goericke, R.,
718 Anderson, C. R., Benitez-Nelson, C. and Whitney, F. A.: Changes in source waters to the
719 Southern California Bight, *Deep Sea Res. Part II Top. Stud. Oceanogr.*, 112, 42–52,
720 doi:10.1016/j.dsr2.2014.04.009, 2015.
- 721 Bograd, S. J., Schroeder, I., Sarkar, N., Qiu, X., Sydeman, W. J. and Schwing, F. B.: Phenology
722 of coastal upwelling in the California Current, *Geophys. Res. Lett.*, 36(1), 1–5,
723 doi:10.1029/2008GL035933, 2009.
- 724 Booth, J. A. T., McPhee-Shaw, E. E., Chua, P., Kingsley, E., Denny, M., Phillips, R., Bograd, S.
725 J., Zeidberg, L. D. and Gilly, W. F.: Natural intrusions of hypoxic, low pH water into nearshore

- 726 marine environments on the California coast, *Cont. Shelf Res.*, 45, 108–115,
727 doi:10.1016/j.csr.2012.06.009, 2012.
- 728 Bresnahan, P. J., Martz, T. R., Takeshita, Y., Johnson, K. S. and LaShomb, M.: Best practices for
729 autonomous measurement of seawater pH with the Honeywell Durafet, *Methods Oceanogr.*, 9,
730 44–60, 2014.
- 731 Brewer, P. G. and Peltzer, E. T.: Limits to marine life, *Science* (80-.), 324(5925), 347–348,
732 2009.
- 733 Byrne, M., Lamare, M., Winter, D., Dworjanyn, S. A. and Uthicke, S.: The stunting effect of a
734 high CO₂ ocean on calcification and development in sea urchin larvae, a synthesis from the
735 tropics to the poles, *Philos. Trans. R. Soc. B Biol. Sci.*, 368(1627), 1–13,
736 doi:10.1098/rstb.2012.0439, 2013.
- 737 Byrne, R. H., Mecking, S., Feely, R. A. and Liu, X.: Direct observations of basin-wide
738 acidification of the North Pacific Ocean, *Geophys. Res. Lett.*, 37(2), 1–5,
739 doi:10.1029/2009GL040999, 2010.
- 740 Cai, W.-J., Hu, X., Huang, W.-J., Murrell, M. C., Lehrter, J. C., Lohrenz, S. E., Chou, W.-C.,
741 Zhai, W., Hollibaugh, J. T., Wang, Y., Zhao, P., Guo, X., Gundersen, K., Dai, M. and Gong, G.-
742 C.: Acidification of subsurface coastal waters enhanced by eutrophication, *Nat. Geosci.*, 4(11),
743 766–770, doi:10.1038/ngeo1297, 2011.
- 744 Carter, B. R., Radich, J. A., Doyle, H. L. and Dickson, A. G.: An automated system for
745 spectrophotometric seawater pH measurements, *Limnol. Oceanogr. Methods*, 11, 16–27,
746 doi:10.4319/lom.2013.11.16, 2013.
- 747 Clayton, T. D. and Byrne, R. H.: Spectrophotometric seawater pH measurements: total hydrogen
748 ion concentration scale calibration of m-cresol purple and at-sea results, *Deep Sea Res. Part I*
749 *Oceanogr. Res. Pap.*, 40(10), 2115–2129, 1993.
- 750 Connell, S. D. and Russell, B. D.: The direct effects of increasing CO₂ and temperature on non-
751 calcifying organisms: increasing the potential for phase shifts in kelp forests., *Proc. Biol. Sci.*,
752 277(1686), 1409–1415, doi:10.1098/rspb.2009.2069, 2010.
- 753 Dickson, A. G., Sabine, C. L. and Christian, J. R., Eds.: Guide to best practices for ocean CO₂
754 measurements, PICES Special Publication 3., 2007.
- 755 Duarte, C. M., Hendriks, I. E., Moore, T. S., Olsen, Y. S., Steckbauer, A., Ramajo, L.,
756 Carstensen, J., Trotter, J. A. and McCulloch, M.: Is ocean acidification an open-ocean
757 syndrome? Understanding anthropogenic impacts on seawater pH, *Estuaries and Coasts*, 36(2),
758 221–236, doi:10.1007/s12237-013-9594-3, 2013.

- 759 Dufault, A. M., Cumbo, V. R., Fan, T.-Y. and Edmunds, P. J.: Effects of diurnally oscillating
760 pCO₂ on the calcification and survival of coral recruits, *Proc. R. Soc. B Biol. Sci.*, 279(1740),
761 2951–2958, doi:10.1098/rspb.2011.2545, 2012.
- 762 Emerson, S. R.: Accurate measurement of O₂, N₂, and Ar gases in water and the solubility of N₂,
763 *Mar. Chem.*, 64(4), 337–347, doi:10.1016/S0304-4203(98)00090-5, 1999.
- 764 Fassbender, A. J., Sabine, C. L., Feely, R. A., Langdon, C. and Mordy, C. W.: Inorganic carbon
765 dynamics during northern California coastal upwelling, *Cont. Shelf Res.*, 31(11), 1180–1192,
766 doi:10.1016/j.csr.2011.04.006, 2011.
- 767 Feely, R. A., Alin, S. R., Newton, J., Sabine, C. L., Warner, M., Devol, A., Krembs, C. and
768 Maloy, C.: The combined effects of ocean acidification, mixing, and respiration on pH and
769 carbonate saturation in an urbanized estuary, *Estuar. Coast. Shelf Sci.*, 88(4), 442–449,
770 doi:10.1016/j.ecss.2010.05.004, 2010.
- 771 Feely, R. A., Doney, S. C. and Cooley, S. R.: Ocean acidification: present conditions and future
772 changes in a high-CO₂ world, *Oceanography*, 22(4), 36–47, 2009.
- 773 Feely, R. A., Sabine, C. L., Hernandez-Ayon, J. M., Ianson, D. and Hales, B.: Evidence for
774 upwelling of corrosive “acidified” water onto the continental shelf., *Science*, 320(5882), 1490–
775 1492, doi:10.1126/science.1155676, 2008.
- 776 Frankignoulle, M.: A complete set of buffer factors for acid/base CO₂ system in seawater, *J. Mar.*
777 *Syst.*, 5(2), 111–118, 1994.
- 778 Frieder, C. A., Gonzalez, J. P., Bockmon, E. E., Navarro, M. O. and Levin, L. A.: Can variable
779 pH and low oxygen moderate ocean acidification outcomes for mussel larvae?, *Glob. Chang.*
780 *Biol.*, 20(3), 754–64, doi:10.1111/gcb.12485, 2014.
- 781 Frieder, C. A., Nam, S., Martz, T. R. and Levin, L. A.: High temporal and spatial variability of
782 dissolved oxygen and pH in a nearshore California kelp forest, *Biogeosciences*, 9(10), 3917–
783 3930, doi:10.5194/bg-9-3917-2012, 2012.
- 784 Friederich, G. E., Walz, P. M., Burczynski, M. G. and Chavez, F. P.: Inorganic carbon in the
785 central California upwelling system during the 1997 – 1999 El Niño–La Niña event, *Prog.*
786 *Oceanogr.*, 54(1-4), 185–203, 2002.
- 787 Garcia, H. E. and Gordon, L. I.: Oxygen solubility in seawater: better fitting equations, *Limnol.*
788 *Oceanogr.*, 37(6), 1307–1312, 1992.
- 789 Gaylord, B., Hill, T. M., Sanford, E., Lenz, E. A., Jacobs, L. A., Sato, K. N., Russell, A. D. and
790 Hettinger, A.: Functional impacts of ocean acidification in an ecologically critical foundation
791 species, *J. Exp. Biol.*, 214(Pt 15), 2586–2594, 2011.

792 Gazeau, F., Gattuso, J.-P., Greaves, M., Elderfield, H., Peene, J., Heip, C. H. R. and Middelburg,
793 J. J.: Effect of carbonate chemistry alteration on the early embryonic development of the Pacific
794 oyster (*Crassostrea gigas*), PLoS One, 6(8), e23010, doi:10.1371/journal.pone.0023010, 2011.

795 Gooding, R. A., Harley, C. D. G. and Tang, E.: Elevated water temperature and carbon dioxide
796 concentration increase the growth of a keystone echinoderm, Proc. Natl. Acad. Sci. U. S. A.,
797 106(23), 9316–9321, doi:10.1073/pnas.0811143106, 2009.

798 Gruber, N., Hauri, C., Lachkar, Z., Loher, D., Frölicher, T. L. and Plattner, G.-K.: Rapid
799 progression of ocean acidification in the California Current System, Science (80-.), 337(6091),
800 220–223, doi:10.1126/science.1216773, 2012.

801 Gruber, N., Lachkar, Z., Frenzel, H., Marchesiello, P., Münnich, M., McWilliams, J. C., Nagai, T.
802 and Plattner, G.-K.: Eddy-induced reduction of biological production in eastern boundary
803 upwelling systems, Nat. Geosci., 4(11), 787–792, doi:10.1038/ngeo1273, 2011.

804 Gruber, N., Sarmiento, J. L. and Stocker, T. F.: An improved method for detecting anthropogenic
805 CO₂ in the oceans, Global Biogeochem. Cycles, 10(4), 809–837, 1996.

806 Hales, B., Takahashi, T. and Bandstra, L.: Atmospheric CO₂ uptake by a coastal upwelling
807 system, Global Biogeochem. Cycles, 19(1), 1–11, doi:10.1029/2004GB002295, 2005.

808 Hall-Spencer, J. M., Rodolfo-Metalpa, R., Martin, S., Ransome, E., Fine, M., Turner, S. M.,
809 Rowley, S. J., Tedesco, D. and Buia, M.-C.: Volcanic carbon dioxide vents show ecosystem
810 effects of ocean acidification, Nature, 454(7200), 96–99, 2008.

811 Harris, K. E., DeGrandpre, M. D. and Hales, B.: Aragonite saturation state dynamics in a coastal
812 upwelling zone, Geophys. Res. Lett., 40(11), 2720–2725, doi:10.1002/grl.50460, 2013.

813 Hauri, C., Gruber, N., McDonnell, A. M. P. and Vogt, M.: The intensity, duration, and severity
814 of low aragonite saturation state events on the California continental shelf, Geophys. Res. Lett.,
815 40(13), 3424–3428, doi:10.1002/grl.50618, 2013a.

816 Hauri, C., Gruber, N., Vogt, M., Doney, S. C., Feely, R. A., Lachkar, Z., Leinweber, A.,
817 McDonnell, A. M. P., Münnich, M. and Plattner, G.-K.: Spatiotemporal variability and long-term
818 trends of ocean acidification in the California Current System, Biogeosciences, 10(1), 193–216,
819 2013b.

820 Hettinger, A., Sanford, E., Hill, T. M., Russell, A. D., Sato, K. N. S., Hoey, J., Forsch, M., Page,
821 H. N. and Gaylord, B.: Persistent carry-over effects of planktonic exposure to ocean acidification
822 in the Olympia oyster, Ecology, 93(12), 2758–2768, doi:10.1890/12-0567.1, 2012.

823 Van Heuven, S., Pierrot, D., Rae, J. W. B., Lewis, E. and Wallace, D. W. .: MATLAB Program
824 Developed for CO₂ System Calculations. ORNL/CDIAC-105b., ,
825 doi:10.3334/CDIAC/otg.CO2SYS_MATLAB_v1.1, 2011.

- 826 Hijioka, Y., Matsuoka, Y., Nishimoto, H., Masui, M. and Kainuma, M.: Global GHG emissions
827 scenarios under GHG concentration stabilization targets, *J. Glob. Environ. Eng.*, 13, 97–108,
828 2008.
- 829 Hofmann, G. E., Evans, T. G., Kelly, M. W., Padilla-Gamiño, J. L., Blanchette, C. A., Washburn,
830 L., Chan, F., McManus, M. A., Menge, B. A., Gaylord, B., Hill, T. M., Sanford, E., LaVigne, M.,
831 Rose, J. M., Kapsenberg, L. and Dutton, J. M.: Exploring local adaptation and the ocean
832 acidification seascape – studies in the California Current Large Marine Ecosystem,
833 *Biogeosciences*, 11(4), 1053–1064, doi:10.5194/bg-11-1053-2014, 2014.
- 834 Hofmann, G. E., Smith, J. E., Johnson, K. S., Send, U., Levin, L. A., Micheli, F., Paytan, A.,
835 Price, N. N., Peterson, B., Takeshita, Y., Matson, P. G., Crook, E. D., Kroeker, K. J., Gambi, M.
836 C., Rivest, E. B., Frieder, C. A., Yu, P. C. and Martz, T. R.: High-frequency dynamics of ocean
837 pH: a multi-ecosystem comparison, edited by W.-C. Chin, *PLoS One*, 6(12), e28983,
838 doi:10.1371/journal.pone.0028983, 2011.
- 839 Hofmann, G. E. and Todgham, A. E.: Living in the now: physiological mechanisms to tolerate a
840 rapidly changing environment., *Annu. Rev. Physiol.*, 72, 127–45, doi:10.1146/annurev-physiol-
841 021909-135900, 2010.
- 842 Keeling, C. D., Piper, S. C., Bacastow, R. B., Wahlen, M., Whorf, T. P., Heimann, M. and
843 Meijer, H. A.: Atmospheric CO₂ and ¹³CO₂ exchange with the terrestrial biosphere and oceans
844 from 1978 to 2000: observations and carbon cycle implications, in *A history of atmospheric CO₂*
845 *and its effects on plants, animals, and ecosystems*, edited by J. R. Ehleringer, T. E. Cerling, and
846 M. D. Dearing, pp. 83–113, Springer Verlag, New York., 2005.
- 847 Kroeker, K. J., Micheli, F., Gambi, M. C. and Martz, T. R.: Divergent ecosystem responses
848 within a benthic marine community to ocean acidification, *Proc. Natl. Acad. Sci. U. S. A.*,
849 108(35), 14515–14520, doi:10.1073/pnas.1107789108, 2011.
- 850 Langdon, C., Gattuso, J. and Andersson, A.: Measurements of calcification and dissolution of
851 benthic organisms and communities, in *Guide to Best Practices for Ocean Acidification Research*
852 *and Data Reporting*, pp. 213–232, Publications Office of the European Union, Luxembourg.,
853 2010.
- 854 Lauvset, S. K. and Gruber, N.: Long-term trends in surface ocean pH in the North Atlantic, *Mar.*
855 *Chem.*, 162, 71–76, doi:10.1016/j.marchem.2014.03.009, 2014.
- 856 Lee, K., Tong, L. T., Millero, F. J., Sabine, C. L., Dickson, A. G., Goyet, C., Park, G.-H.,
857 Wanninkhof, R., Feely, R. A. and Key, R. M.: Global relationships of total alkalinity with
858 salinity and temperature in surface waters of the world’s oceans, *Geophys. Res. Lett.*, 33(19), 1–
859 5, doi:10.1029/2006GL027207, 2006.
- 860 Leinweber, A. and Gruber, N.: Variability and trends of ocean acidification in the Southern
861 California Current System: a time series from Santa Monica Bay, *J. Geophys. Res. Ocean.*,
862 118(7), 3622–3633, doi:10.1002/jgrc.20259, 2013.

- 863 Leinweber, A., Gruber, N., Frenzel, H., Friederich, G. E. and Chavez, F. P.: Diurnal carbon
864 cycling in the surface ocean and lower atmosphere of Santa Monica Bay, California, *Geophys.*
865 *Res. Lett.*, 36(8), 3–7, doi:10.1029/2008GL037018, 2009.
- 866 Liu, X., Patsavas, M. C. and Byrne, R. H.: Purification and characterization of meta-cresol
867 purple for spectrophotometric seawater pH measurements, *Environ. Sci. Technol.*, 45(11), 4862–
868 4868, doi:10.1021/es200665d, 2011.
- 869 Lueker, T. J., Dickson, A. G. and Keeling, C. D.: Ocean pCO₂ calculated from dissolved
870 inorganic carbon, alkalinity, and equations for K₁ and K₂: validation based on laboratory
871 measurements of CO₂ in gas and seawater at equilibrium, *Mar. Chem.*, 70(1-3), 105–119,
872 doi:10.1016/S0304-4203(00)00022-0, 2000.
- 873 Martz, T. R., Connery, J. G. and Johnson, K. S.: Testing the Honeywell Durafet for seawater pH
874 applications, *Limnol. Oceanogr. Methods*, 8, 172–184, doi:10.4319/lom.2010.8.172, 2010.
- 875 Martz, T. R., Send, U., Ohman, M. D., Takeshita, Y., Bresnahan, P., Kim, H.-J. and Nam, S.:
876 Dynamic variability of biogeochemical ratios in the Southern California Current System,
877 *Geophys. Res. Lett.*, 41(7), 2496–2501, doi:10.1002/2014GL059332, 2014.
- 878 Martz, T. R., Takeshita, Y., Rolph, R. and Bresnahan, P.: Tracer monitored titrations:
879 measurement of dissolved oxygen., *Anal. Chem.*, 84(1), 290–296, doi:10.1021/ac202537f, 2012.
- 880 Matsumoto, K. and Gruber, N.: How accurate is the estimation of anthropogenic carbon in the
881 ocean? An evaluation of the ΔC^* method, *Global Biogeochem. Cycles*, 19(3), 1–17,
882 doi:10.1029/2004GB002397, 2005.
- 883 McElhany, P. and Busch, D. S.: Appropriate pCO₂ treatments in ocean acidification experiments,
884 *Mar. Biol.*, 160(8), 1807–1812, doi:10.1007/s00227-012-2052-0, 2013.
- 885 McNeil, B. I. and Matear, R. J.: Southern Ocean acidification: a tipping point at 450-ppm
886 atmospheric CO₂, *Proc. Natl. Acad. Sci. U. S. A.*, 105(48), 18860–18864,
887 doi:10.1073/pnas.0806318105, 2008.
- 888 Mehrbach, C., Culberson, C. H., Hawley, J. E. and Pytkowicz, R. M.: Measurement of the
889 apparent dissociation constants of carbonic acid in seawater at atmospheric pressure, *Limnol.*
890 *Oceanogr.*, 18(6), 897–907, doi:10.4319/lo.1973.18.6.0897, 1973.
- 891 Nam, S., Kim, H.-J. and Send, U.: Amplification of hypoxic and acidic events by La Niña
892 conditions on the continental shelf off California, *Geophys. Res. Lett.*, 38(22), 1–5,
893 doi:10.1029/2011GL049549, 2011.
- 894 Nam, S., Takeshita, Y., Frieder, C. A., Martz, T. and Ballard, J.: Seasonal advection of Pacific
895 Equatorial Water alters oxygen and pH in the Southern California Bight, *J. Geophys. Res.*
896 *Ocean.*, 120, n/a–n/a, doi:10.1002/2015JC010859, 2015.

- 897 Navarro, M. O.: Consequences of environmental variability for spawning and embryo
898 development of inshore market squid *Doryteuthis opalescens*, Ph.D. thesis, University of
899 California San Diego. Ann Arbor, USA, ProQuest Dissertations and Theses (Publication No.
900 3644287)., 2014.
- 901 Navarro, M. O., Parnell, P. E. and Levin, L. A.: Year-round spawning of the Market Squid,
902 *Doryteuthis opalescens* and associated critical habitat along an upwelling margin, in Coastal and
903 Estuarine Research Federation National Conference, San Diego., 2013.
- 904 O’Sullivan, D. W. and Millero, F. J.: Continual measurement of the total inorganic carbon in
905 surface seawater, *Mar. Chem.*, 60(1-2), 75–83, doi:10.1016/S0304-4203(97)00079-0, 1998.
- 906 Padilla-Gamiño, J. L., Kelly, M. W., Evans, T. G. and Hofmann, G. E.: Temperature and CO₂
907 additively regulate physiology, morphology and genomic responses of larval sea urchins,
908 *Strongylocentrotus purpuratus*, *Proc. R. Soc. B Biol. Sci.*, 280(1759), 20130155,
909 doi:10.1098/rspb.2013.0155, 2013.
- 910 Pineda, J.: Predictable upwelling and the shoreward transport of planktonic larvae by internal
911 tidal bores, *Science* (80-.), 253(5019), 548–551, 1991.
- 912 Price, N. N., Martz, T. R., Brainard, R. E. and Smith, J. E.: Diel variability in seawater pH relates
913 to calcification and benthic community structure on coral reefs, *PLoS One*, 7(8), e43843,
914 doi:10.1371/journal.pone.0043843, 2012.
- 915 Reum, J. C. P., Alin, S. R., Feely, R. A., Newton, J., Warner, M. and McElhany, P.: Seasonal
916 carbonate chemistry covariation with temperature, oxygen, and salinity in a fjord estuary:
917 Implications for the design of ocean acidification experiments, *PLoS One*, 9(2), e89619,
918 doi:10.1371/journal.pone.0089619, 2014.
- 919 Reum, J. C. P., Alin, S. R., Harvey, C. J., Bednarsek, N., Evans, W., Feely, R. A., Hales, B.,
920 Lucey, N., Mathis, J. T., McElhany, P., Newton, J., Newton, J. and Sabine, C. L.: Interpretation
921 and design of ocean acidification experiments in upwelling systems in the context of carbonate
922 chemistry co-variation with temperature and oxygen, *ICES J. Mar. Sci.*, 528–536,
923 doi:10.1093/icesjms/fsu231, 2015.
- 924 Rivkin, R. B. and Legendre, L.: Biogenic carbon cycling in the upper ocean: effects of microbial
925 respiration., *Science*, 291(5512), 2398–2400, doi:10.1126/science.291.5512.2398, 2001.
- 926 Rodolfo-Metalpa, R., Houlbrèque, F., Tambutté, É., Boisson, F., Baggini, C., Patti, F. P., Jeffree,
927 R., Fine, M., Foggo, a., Gattuso, J.-P. and Hall-Spencer, J. M.: Coral and mollusc resistance to
928 ocean acidification adversely affected by warming, *Nat. Clim. Chang.*, 1(6), 308–312,
929 doi:10.1038/nclimate1200, 2011.
- 930 Rykaczewski, R. R. and Dunne, J. P.: Enhanced nutrient supply to the California Current
931 Ecosystem with global warming and increased stratification in an earth system model, *Geophys.*
932 *Res. Lett.*, 37(21), 1–5, doi:10.1029/2010GL045019, 2010.

- 933 Sabine, C. L., Feely, R. A., Key, R. M., Bullister, J. L., Millero, F. J., Lee, K., Peng, T.-H.,
934 Tilbrook, B., Ono, T. and Wong, C. S.: Distribution of anthropogenic CO₂ in the Pacific Ocean,
935 *Global Biogeochem. Cycles*, 16(4), 1–17, doi:10.1029/2001GB001639, 2002.
- 936 Sabine, C. L. and Tanhua, T.: Estimation of anthropogenic CO₂ inventories in the ocean, *Ann.*
937 *Rev. Mar. Sci.*, 2(1), 175–198, doi:10.1146/annurev-marine-120308-080947, 2010.
- 938 Send, U. and Nam, S.: Relaxation from upwelling: the effect on dissolved oxygen on the
939 continental shelf, *J. Geophys. Res.*, 117(4), 1–9, doi:10.1029/2011JC007517, 2012.
- 940 Smith, T. M., Reynolds, R. W., Peterson, T. C. and Lawrimore, J.: Improvements to NOAA’s
941 historical merged land–ocean surface temperature analysis (1880–2006), *J. Clim.*, 21(10), 2283–
942 2296, doi:10.1175/2007JCLI2100.1, 2008.
- 943 Somero, G. N.: Thermal physiology and vertical zonation of intertidal animals: optima, limits,
944 and costs of living, *Integr. Comp. Biol.*, 42(4), 780–789, 2002.
- 945 Sunda, W. G. and Cai, W.-J.: Eutrophication induced CO₂-acidification of subsurface coastal
946 waters: interactive effects of temperature, salinity, and atmospheric pCO₂, *Environ. Sci.*
947 *Technol.*, 46(19), 10651–10659, doi:10.1021/es300626f, 2012.
- 948 Sutton, A. J., Feely, R. A., Sabine, C. L., McPhaden, M. J., Takahashi, T., Chavez, F. P.,
949 Friederich, G. E. and Mathis, J. T.: Natural variability and anthropogenic change in equatorial
950 Pacific surface ocean pCO₂ and pH, *Global Biogeochem. Cycles*, 28(2), 1–15,
951 doi:10.1002/2013GB004679, 2014.
- 952 Swart, N. C., Allen, S. E. and Greenan, B. J. W.: Resonant amplification of subinertial tides in a
953 submarine canyon, *J. Geophys. Res.*, 116(9), 1–14, doi:10.1029/2011JC006990, 2011.
- 954 Waldbusser, G. G., Hales, B., Langdon, C. J., Haley, B. A., Schrader, P., Brunner, E. L., Gray, M.
955 W., Miller, C. A. and Gimenez, I.: Saturation-state sensitivity of marine bivalve larvae to ocean
956 acidification, *Nat. Clim. Chang.*, 5, 273–280, doi:10.1038/NCLIMATE2479, 2015.
- 957

958 Table 1: Summary of sensor deployments

Habitat Type	Deployment Site	DD ^a	BD ^b	Latitude	Longitude	Days ^c
Surf Zone	Scripps Pier	4	6	32.87°N	117.26°W	122
Kelp Forest	La Jolla Kelp Forest	17	20	32.81°N	117.29°W	128
Canyon Edge ^d	La Jolla Canyon	30	30	32.86°N	117.27°W	302
Shelf Break	Del Mar Buoy	88	100	32.94°N	117.32°W	335

959 ^a Sensor deployment depth in meters

960 ^b Bottom depth in meters

961 ^c Total deployment days between June 2012 and June 2013.

962 ^d A linear drift correction for salinity was applied for 2 of the 4 deployments.

963

964 Table 2. Mean \pm s.d of modeled carbonate parameters at in situ conditions for preindustrial, 2012,
 965 2060, and 2100 using the RCP6.0 projection at each habitat.

	Year	pCO ₂ (μ atm)	Ω_{Ar}	pH
Surf Zone (4m)	Preind.	267 \pm 26	3.09 \pm 0.21	8.19 \pm 0.034
	2012	394 \pm 43	2.38 \pm 0.25	8.05 \pm 0.038
	2060	473 \pm 56	2.09 \pm 0.19	7.98 \pm 0.041
	2100	619 \pm 80	1.71 \pm 0.18	7.88 \pm 0.045
Kelp Forest (17 m)	Preind.	365 \pm 74	2.28 \pm 0.42	8.08 \pm 0.078
	2012	516 \pm 108	1.77 \pm 0.36	7.95 \pm 0.083
	2060	683 \pm 156	1.43 \pm 0.33	7.84 \pm 0.094
	2100	937 \pm 231	1.11 \pm 0.29	7.72 \pm 0.105
Canyon Edge (30 m)	Preind.	365 \pm 68	2.29 \pm 0.37	8.08 \pm 0.068
	2012	529 \pm 105	1.75 \pm 0.31	7.94 \pm 0.075
	2060	702 \pm 155	1.40 \pm 0.29	7.83 \pm 0.085
	2100	964 \pm 231	1.09 \pm 0.25	7.70 \pm 0.095
Shelf Break (88 m)	Preind.	637 \pm 132	1.38 \pm 0.27	7.86 \pm 0.083
	2012	878 \pm 149	1.05 \pm 0.18	7.73 \pm 0.070
	2060	1195 \pm 200	0.80 \pm 0.15	7.61 \pm 0.070
	2100	1639 \pm 246	0.60 \pm 0.10	7.47 \pm 0.065

966

967

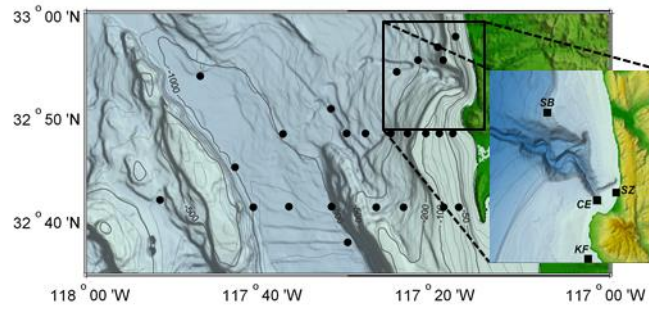
968 Table 3. Mean daily range of carbonate parameters at in situ conditions for 2012 at each habitat.

	pCO₂ (μatm)	Ω_{Ar}	pH
Surf Zone	96	0.46	0.085
Kelp Forest	68	0.22	0.054
Canyon Edge	167	0.48	0.120
Shelf Break	110	0.14	0.053

969

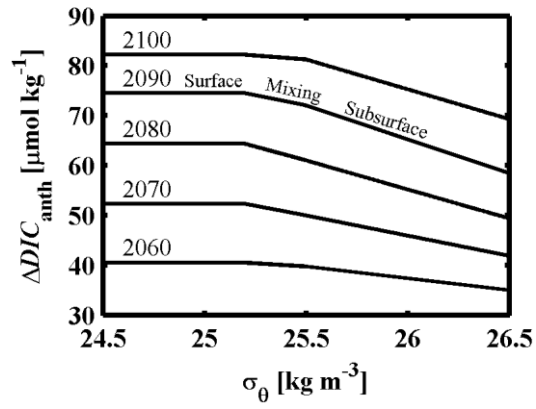
970

971



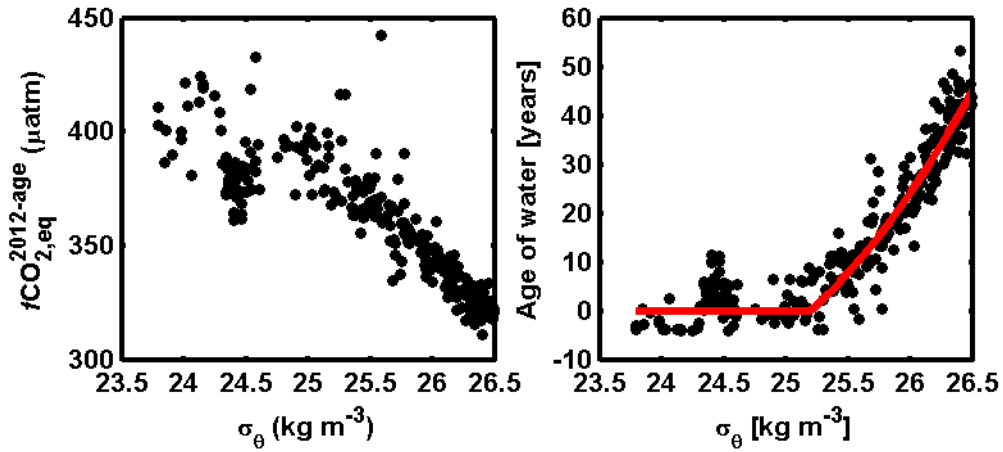
972

973 Figure 1: Map of study region. Hydrographic stations (black dots) and sensor deployment sites
974 (black squares) are shown. Initials are: CE = canyon edge, SB = shelf break, SZ = surf zone, and
975 KF = kelp forest.
976



977

978 Figure 2: ΔDIC_{anth} as a function of σ_{θ} for certain modeled years (indicated above line) using the
 979 ICPP RCP6.0 projection. The three regimes used in this model, surface, mixing, and subsurface,
 980 are labeled.
 981

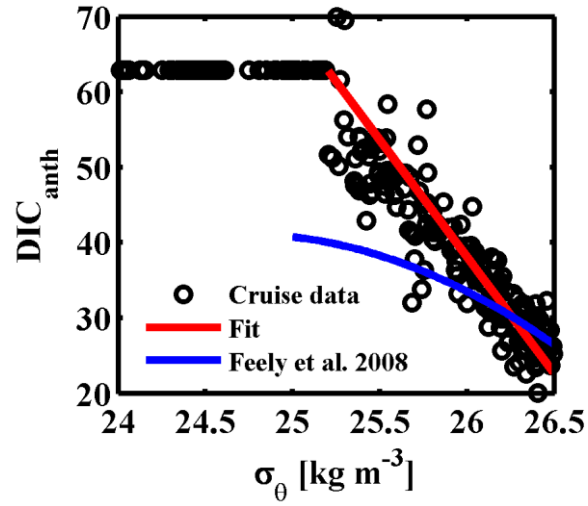


982

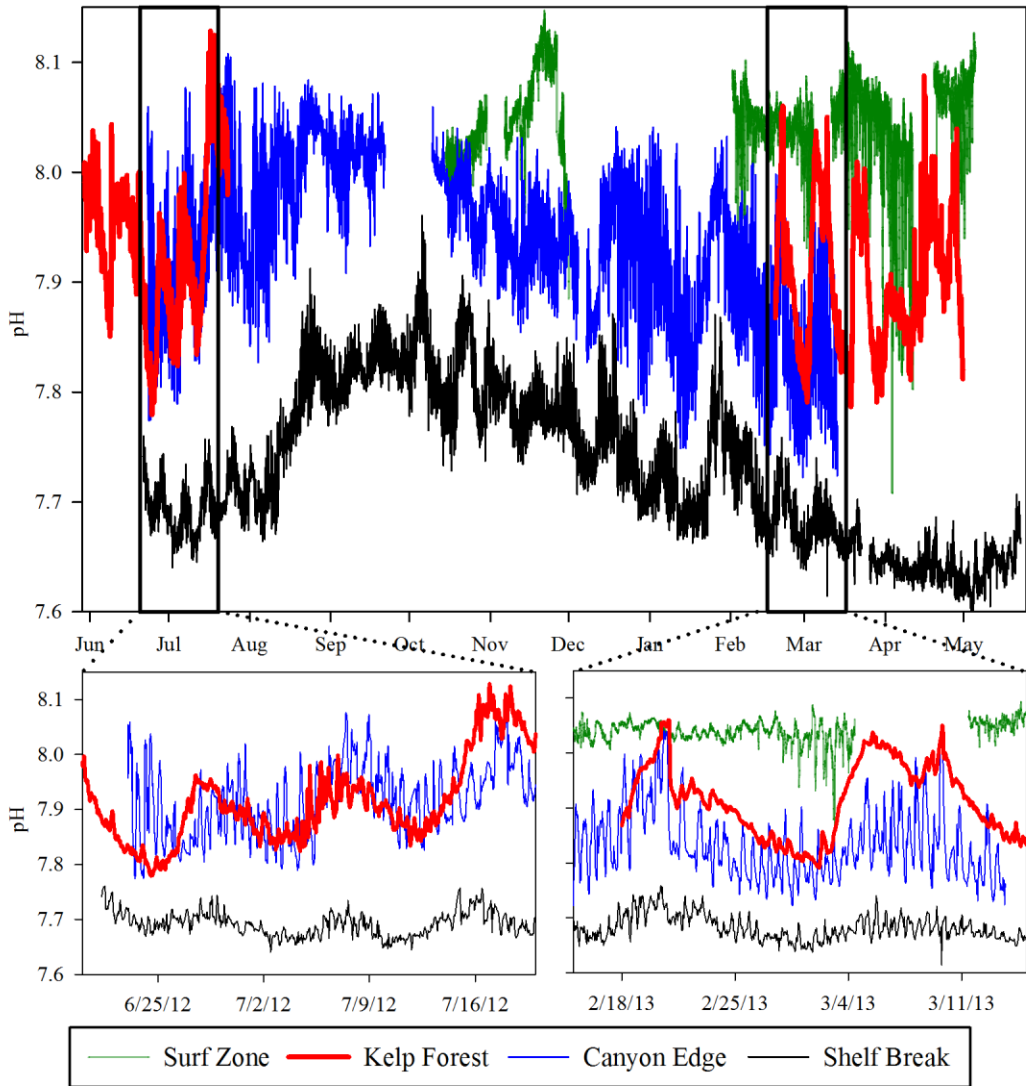
983 Figure 3: $f\text{CO}_{2,\text{eq}}^{2012-\text{age}}$ calculated from hydrographic data (left) and the calculated age- σ_θ
 984 relationship (right) is shown. Good agreement ($R^2 = 0.87$) between the data (black circles) and
 985 the fit (age = $8.852(\sigma_\theta - 25.2)^2 + 23.132(\sigma_\theta - 25.2)$; red line) is observed (right). Age of surface
 986 waters ($\sigma_\theta < 25.2 \text{ kg m}^{-3}$) was assumed to be 0.
 987

988

989



990
 991 Figure 4: DIC_{anth} as a function of σ_{θ} . The calculated values and the fit are represented by black
 992 circles and a red line, respectively. The blue line shows DIC_{anth} using the formulations from
 993 Feely et al. (2008).
 994

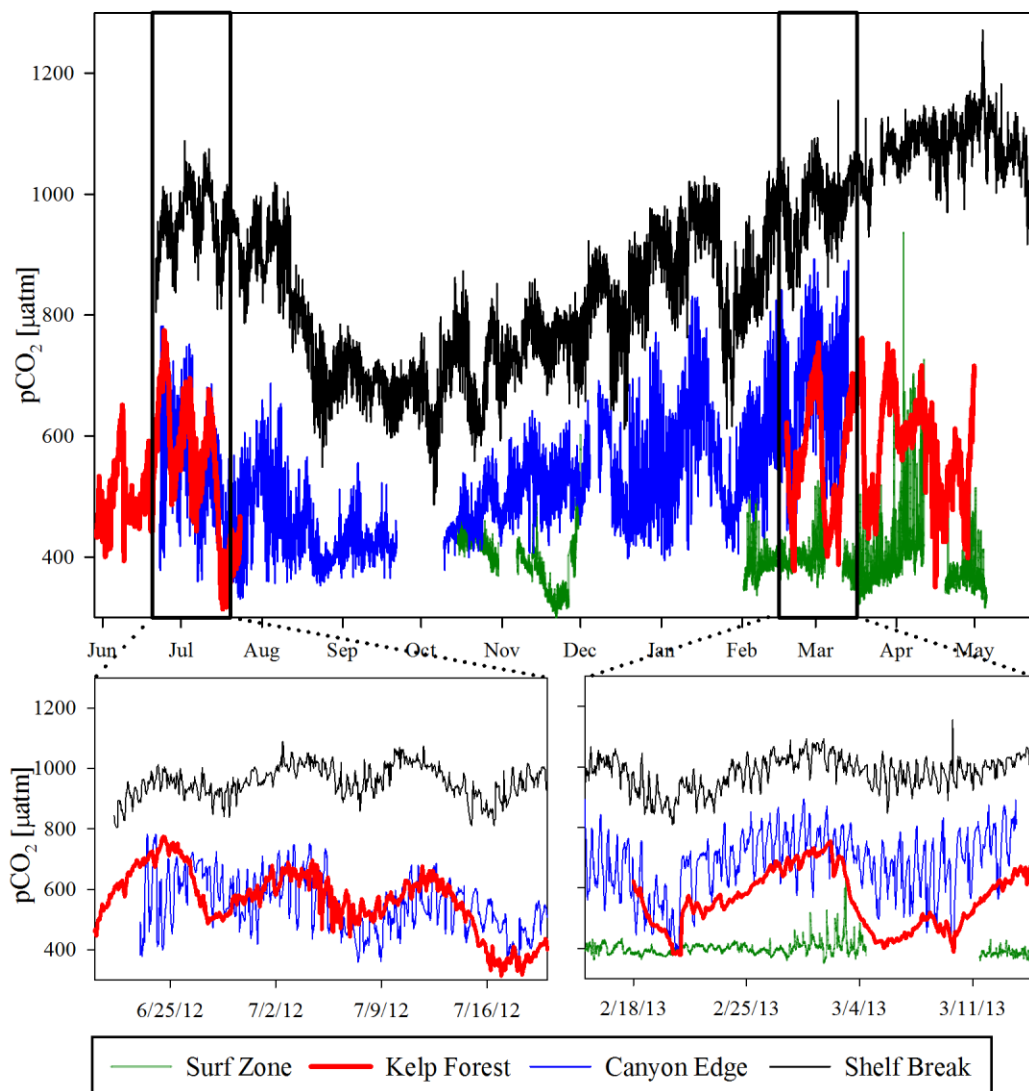


995

996 Figure 5: Time series of sensor pH between June 2012 to June. Two lower panels are month-long
 997 snapshots. pH is reported at in situ conditions.

998

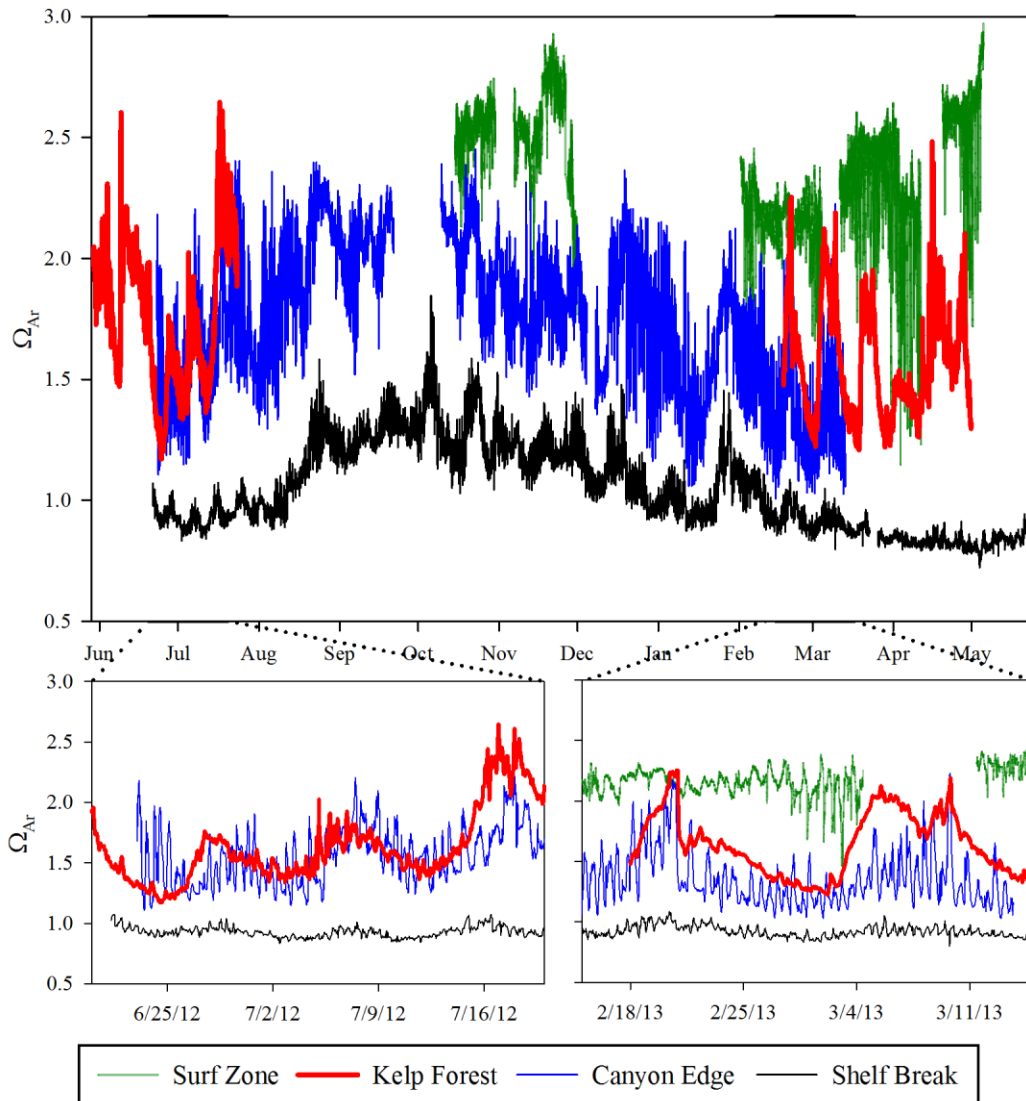
999



1000

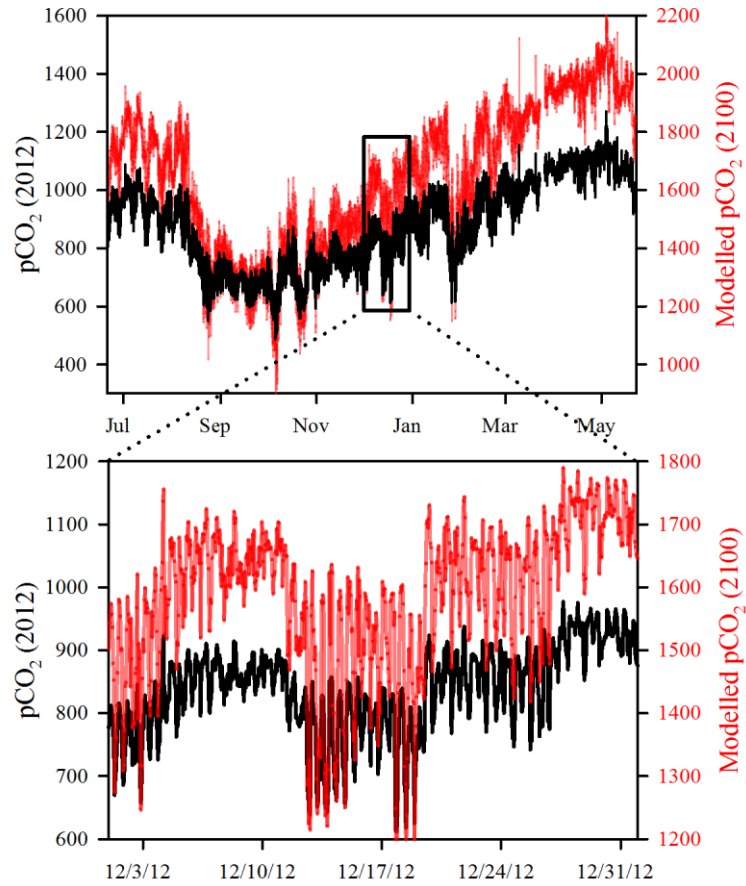
1001 Figure 6: Time series of $p\text{CO}_2$ calculated from sensor pH and TA^{est} between June 2012 to June
 1002 2013. Two lower panels are month-long snapshots. $p\text{CO}_2$ is reported at in situ conditions.

1003



1004
 1005
 1006
 1007

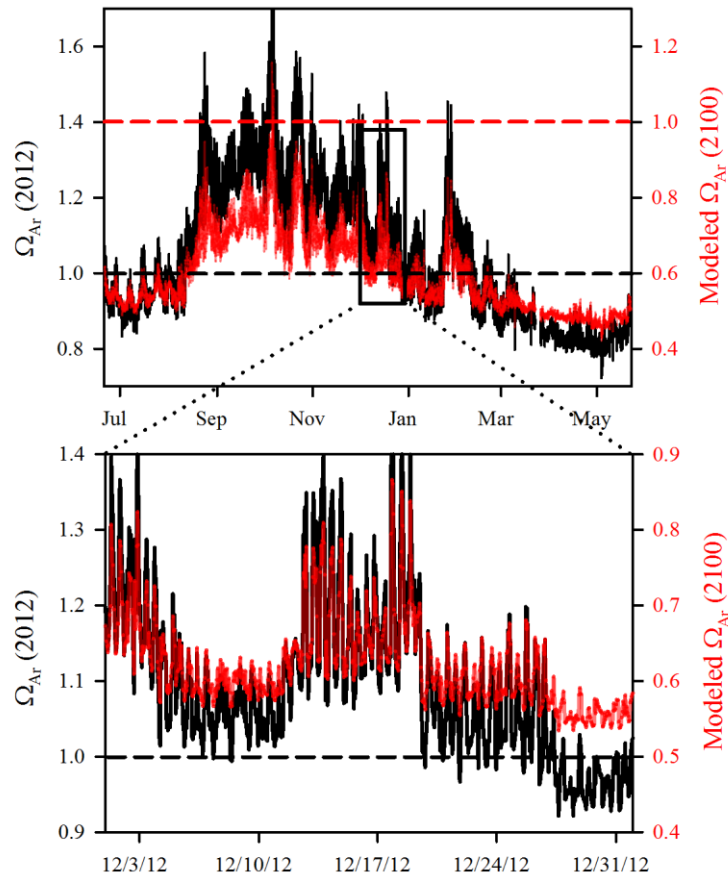
Figure 7: Time series of Ω_{Ar} calculated from sensor pH and TA^{est} between June 2012 to June 2013. Two lower panels are month-long snapshots. Ω_{Ar} is reported at in situ conditions.



1008

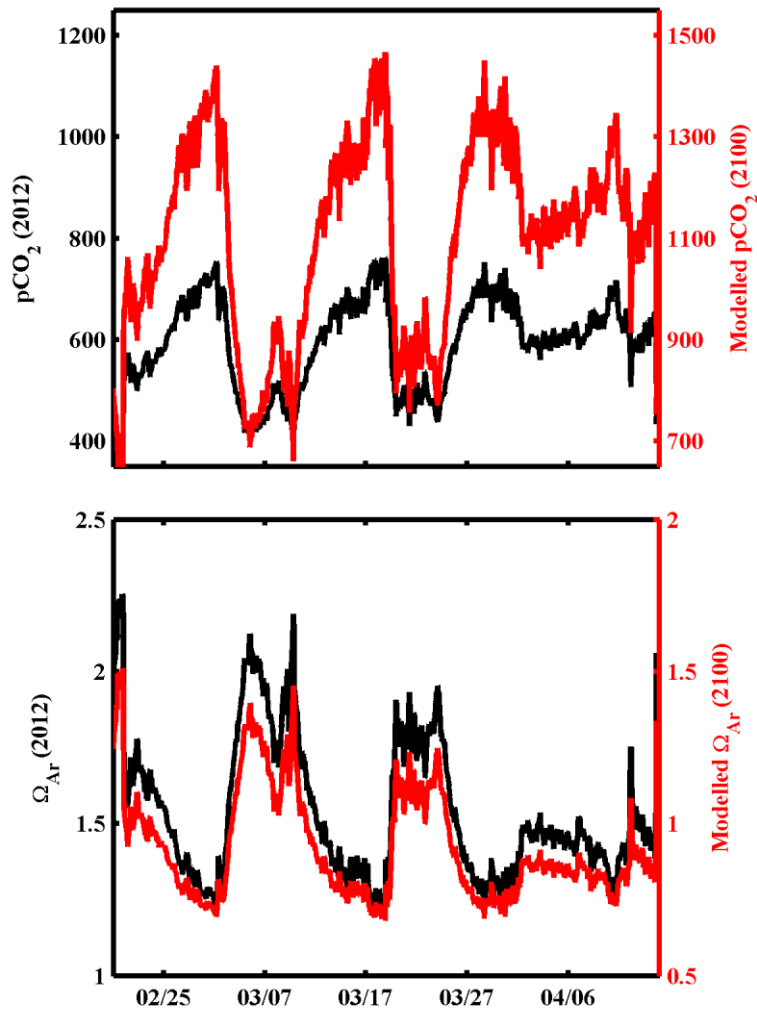
1009 Figure 8: Observed pCO₂ in 2012 (black) and modeled pCO₂ using the IPCC RCP 6.0 scenario
 1010 for the year 2100 (red) at the Del Mar Buoy (88 m) over an annual cycle (top). A close up for the
 1011 month of December is shown on the bottom. Note that the range, but not the absolute values, of
 1012 the vertical axes for each figure is the same.

1013

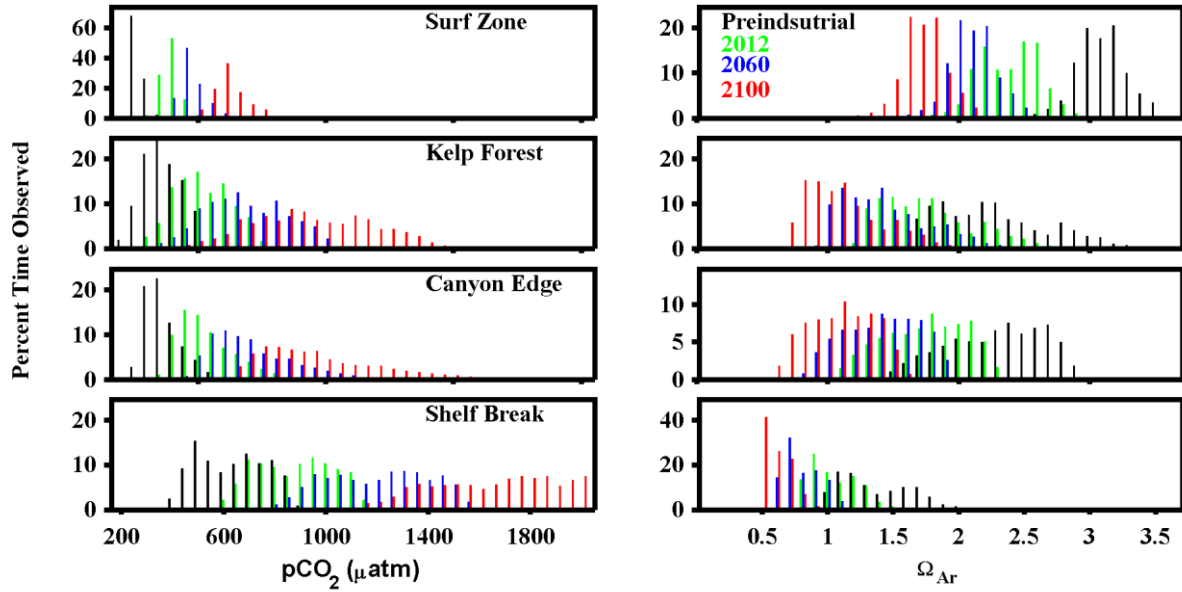


1014

1015 Figure 9: Observed Ω_{Ar} in 2012 (black) and modeled Ω_{Ar} using the IPCC RCP6.0 scenario for
 1016 the year 2100 (red) at the shelf break (88 m) over an annual cycle (top). A close up for the month
 1017 of December is shown on the bottom. Dashed lines represent $\Omega_{Ar} = 1$. Note that the range, but
 1018 not the absolute values, of the vertical axes for each figure is the same.
 1019

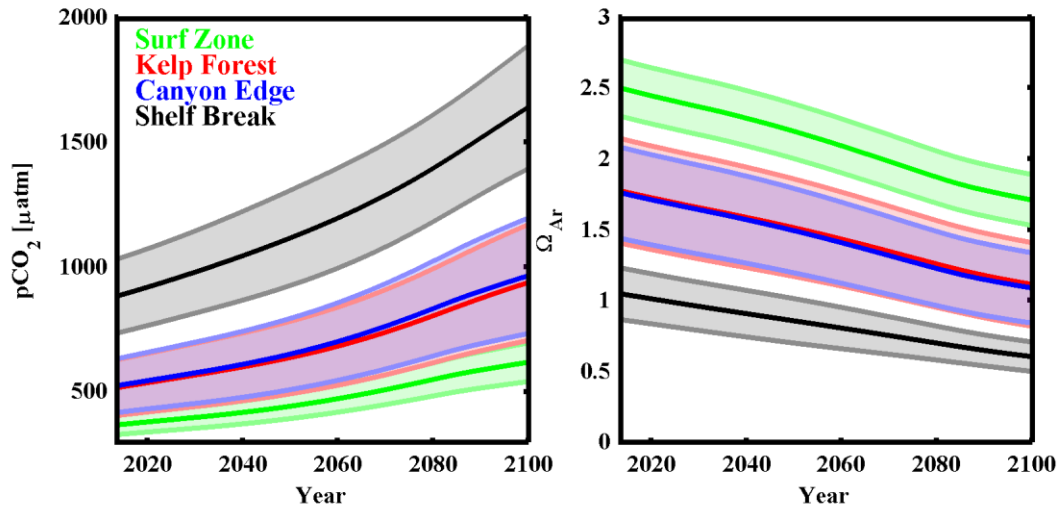


1020
 1021 Figure 10: Observed (black) and modelled (red) $p\text{CO}_2$ (top) and Ω_{Ar} (bottom) at the La Jolla kelp
 1022 forest (17 m). Modelled values correspond to projected values in 2100 using the IPCC RCP6.0
 1023 scenario. Note that the range, but not the absolute values, of the vertical axes for each figure is
 1024 the same.
 1025



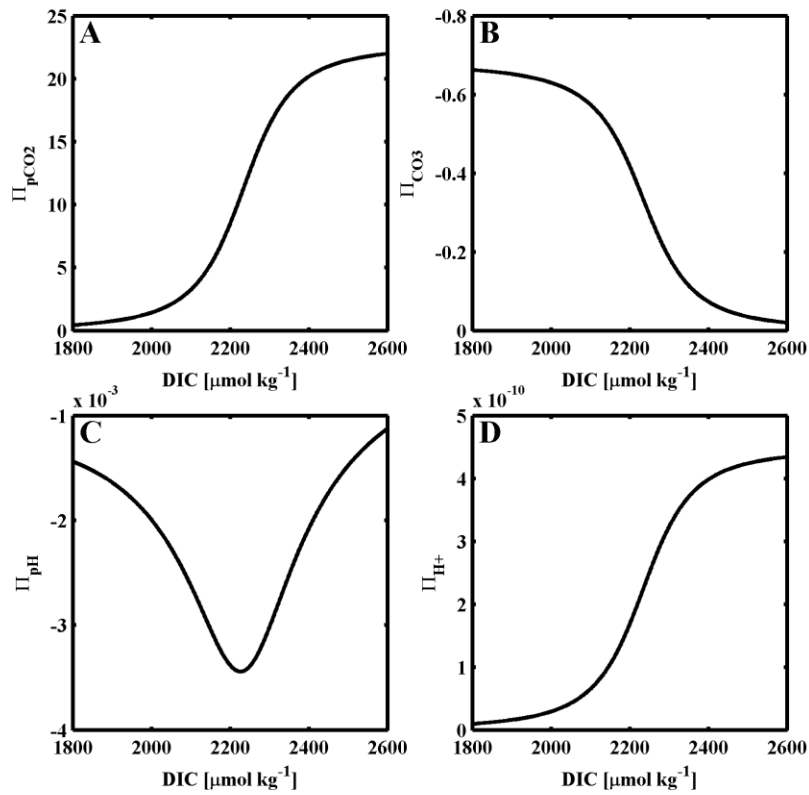
1026

1027 Figure 11: Histogram of modeled pCO₂ (left) and Ω_{Ar} (right) distribution at the four depths for
 1028 preindustrial (black), 2012 (green), 2060 (blue), and 2100 (red). Atmospheric pCO₂ for the years
 1029 2060 and 2100 roughly correspond to 510 and 670 μatm based on the IPCC RCP6.0 scenario.
 1030



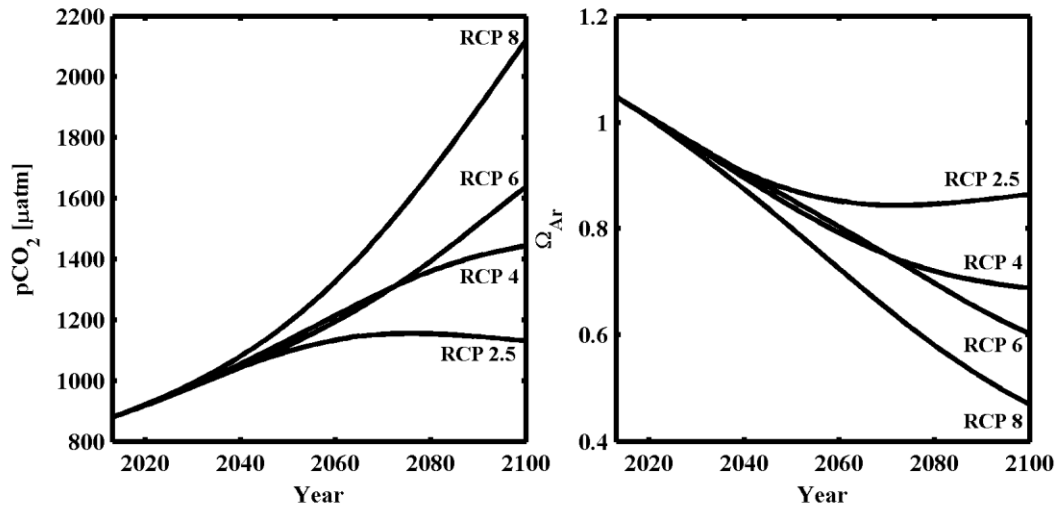
1031

1032 Figure 12: Projected pCO₂ (left) and Ω_{Ar} (right) between 2013 and 2100 under the IPCC RCP6.0
 1033 scenario. The solid line and the shaded region represent the mean and ± 1 s.d., respectively.
 1034



1035

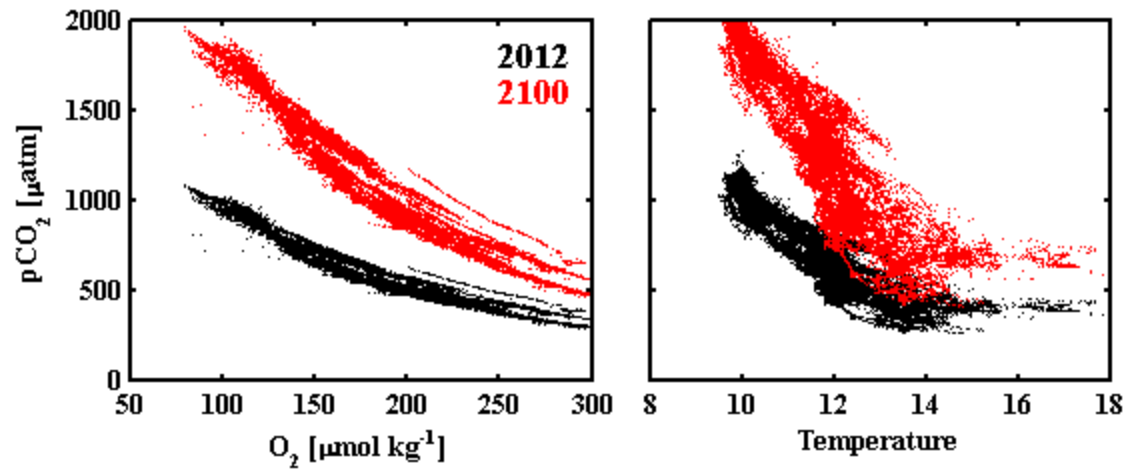
1036 Figure 13: Buffer factor Π for pCO_2 (A), CO_3^{2-} (B), pH (C), and $[\text{H}^+]$ (D) as a function of DIC.
 1037 Note the inverted y axis in panels B and C. Model parameters to calculate the Π values were: TA
 1038 = $2240 \mu\text{mol kg}^{-1}$, temperature = 10°C , salinity = 33.5 , pressure = 1.013 bar .
 1039



1040

1041 Figure 14: Projections of mean pCO₂ (left) and Ω_{Ar} (right) at the shelf break (88 m) based on
 1042 four projections from the Fifth Assessment of the IPCC.

1043



1044

1045 Figure 15: pCO₂ as a function of O₂ (left) and temperature (right) from the kelp forest and shelf
1046 break. Data observed in 2012 and projected for 2100 are plotted.
1047